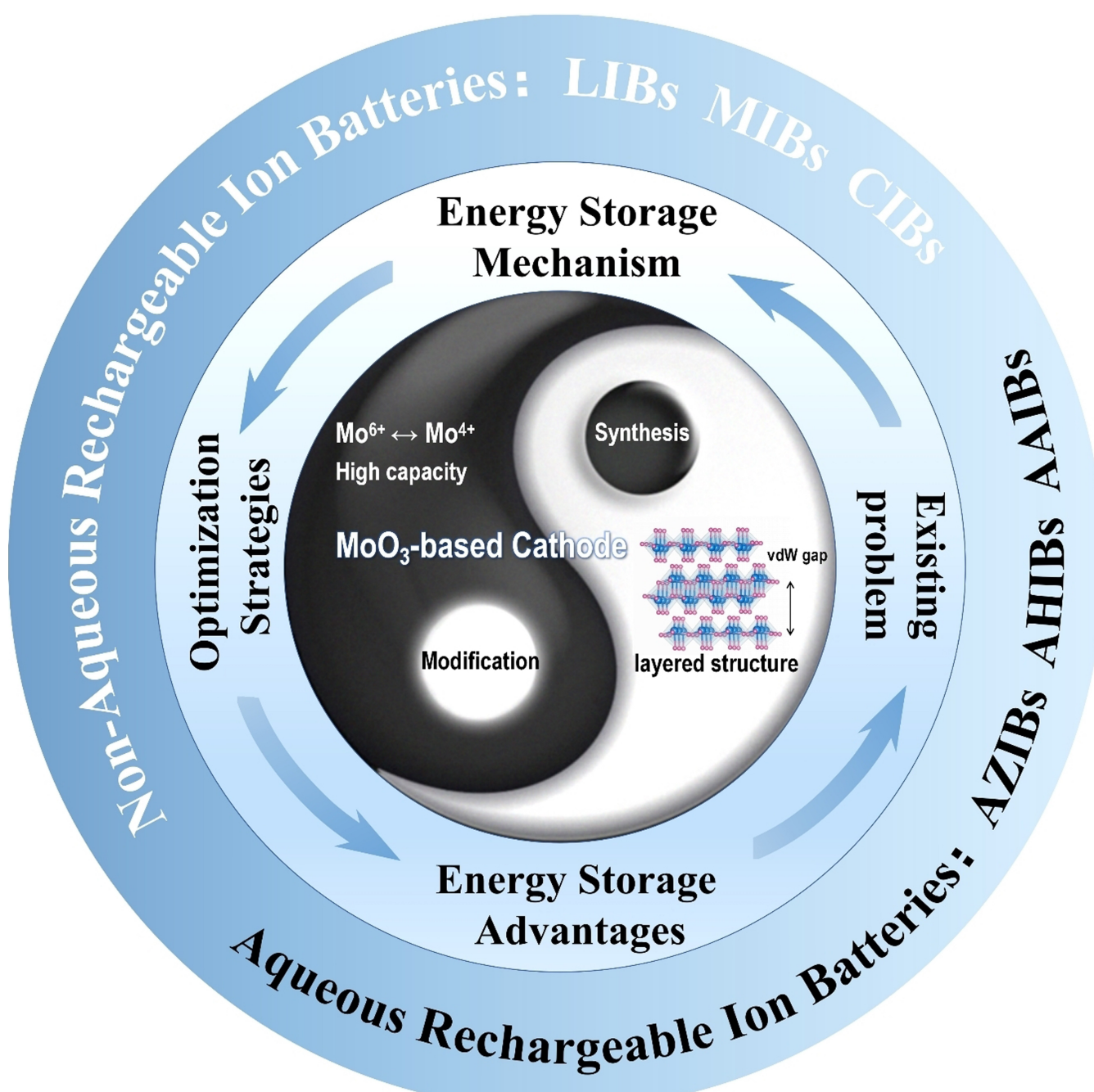


# Intercalation Reaction of Molybdenum Trioxide Cathode for Rechargeable Ion Batteries

Dawei Sheng,<sup>[a, b]</sup> Xiaoxu Liu,<sup>\*[b]</sup> Qiang Zhang,<sup>\*[a]</sup> Haozhe Yi,<sup>[c]</sup> Xuanzhang Wang,<sup>[a]</sup> Shufang Fu,<sup>[a]</sup> Sheng Zhou,<sup>[a]</sup> Jiaguo Shen,<sup>[a]</sup> and Ang Gao<sup>[a]</sup>



Based on the intercalation reaction, molybdenum trioxide has become an attractive cathode material for rechargeable ion batteries owing to its high theoretical capacity and layered structure. This review summarizes the recent research progress of molybdenum trioxide-based cathode in non-aqueous lithium, magnesium, calcium-ion batteries, aqueous zinc, hydrogen, and aluminum-ion batteries, focusing on the energy storage mechanism, existing problems, and optimization strategies in

rechargeable ion batteries. Finally, the perspectives about challenges and future further development directions of molybdenum trioxide cathode in electrochemical energy storage are proposed. This review will comprehensively summarize molybdenum trioxide as a cathode in rechargeable ion batteries and clarify its practical application prospects for sustainable development.

## 1. Introduction

In the past few decades, with the development of the economy and the accretion of industrialization advancement, global energy consumption has increased significantly. It is urgent to develop sustainable energy, and the general trend of the future is to increase the proportion of renewable energy power generation and realize the electrification of transportation. The development and application of electrochemical energy storage systems play a vital role in achieving these goals.<sup>[1]</sup> Among electrochemical energy storage systems, environmentally friendly, low-cost rechargeable ion batteries include lithium-ion batteries, emerging metal ion batteries, and non-metallic ion batteries. Lithium-ion batteries (LIBs), also known as "rocking chair batteries," realize energy conversion and storage through reversible intercalation-deintercalation of lithium-ions ( $\text{Li}^+$ ) between the cathode (positive electrode) and anode (negative electrode). Since Sony commercialized LIBs in the 1990s, LIBs have become one of the most widespread rechargeable batteries. Because LIBs have the advantages of high energy density, no memory effect, and no capacity loss when not in use, LIBs are widely used in portable electronic products such as laptops, mobile phones, and digital cameras.<sup>[2]</sup> Moreover, the development of LIBs has further stimulated the demand for electric vehicles (EVs) and hybrid electric vehicles (HEVs).<sup>[3]</sup> The limited lithium resources, potential price spike, and higher energy density requirements put LIBs under constant debate. Multivalent metal ion batteries<sup>[4]</sup> (such as magnesium-ion, calcium-ion, zinc-ion, and aluminum-ion batteries) with better safety, more abundant reserves, higher volume energy density, and non-metallic ions with smaller ion radius and wider

availability (such as hydrogen-ion batteries) become potential candidates.<sup>[5]</sup> Multivalent metal cations as charge carriers shuttle back and forth between cathode and anode electrodes during charge and discharge cycles. This working principle is similar to LIBs, which means that the understanding and manufacturing experience of LIBs can be applied to the rapid development of multivalent metal-ion batteries.<sup>[6]</sup> Rechargeable batteries by whether the electrolyte is water as a solvent divided into aqueous and non-aqueous rechargeable ion batteries.<sup>[7]</sup> Compared with non-aqueous rechargeable ion batteries, aqueous rechargeable ion batteries have obvious safety and environmental protection advantages, and the price is lower. But the narrow electrochemical stability window is not conducive to high energy density, and the cycle life still needs to be improved. Non-aqueous rechargeable ion batteries tend to have a wider operating voltage window, which can ensure the high energy density of energy storage devices. Among them, the non-aqueous magnesium and calcium-ion batteries use magnesium and calcium metal as anode materials, which have much higher volume-specific capacity than lithium metal. Magnesium and calcium resources are abundant (Mg: 8, Ca: 5, Li: 33), lower price (Mg: 2.2, Ca: 2.28, Li: 19.2 USD kg<sup>-1</sup>), moderate reduction potential (Mg: -2.356, Ca: -2.84, Li: -3.04 V vs. SHE.), is one of the "post-lithium system" battery candidates. Zinc-ion and aluminum-ion batteries use non-toxic, non-flammable, and low-volatile electrolytes in aqueous rechargeable ion batteries. Furthermore, compared with organic electrolytes, aqueous electrolytes have advantages in ionic conductivity, interfacial wettability, and environmental friendliness.<sup>[8]</sup> At the same time, zinc-ions and aluminum-ions can use as charge carriers for multi-electron reactions with higher volume capacity ( $\text{Li}^+$ : 2.04 A h cm<sup>-3</sup>,  $\text{Zn}^{2+}$ : 5.86 A h cm<sup>-3</sup>,  $\text{Al}^{3+}$ : 8.05 A h cm<sup>-3</sup>), which is an ideal choice for large-scale energy storage applications. In addition, in aqueous hydrogen-ion batteries with non-metallic ions as charge carriers, the hydrogen ions have an ionic radius much smaller than the metal ions. They are based on the Grothuss proton fast transport mechanism, resulting in a better rate and cycle performance.<sup>[9]</sup>

The electrochemical performance and production cost of rechargeable ion batteries depend heavily on the electrode materials.<sup>[10]</sup> The potential difference between the cathode and anode and the charge storage of the electrode determines the energy density. The ions' diffusion rate and reaction kinetics in the electrode determines the power density. As a critical component of rechargeable ion batteries, the cathode largely

[a] D. Sheng, Prof. Q. Zhang, Prof. X. Wang, Prof. S. Fu, Prof. S. Zhou, J. Shen, A. Gao  
Institution Key Laboratory for Photonic and Electronic Bandgap Materials  
Ministry of Education, School of Physics and Electronic Engineering  
Harbin Normal University  
Harbin, 150025 (China)

E-mail: hsdzq80@126.com

[b] D. Sheng, Prof. X. Liu  
School of Materials Science and Engineering  
Shaanxi Key Laboratory of Green Preparation and Functionalization for  
Inorganic Materials  
Shaanxi University of Science and Technology  
Xi'an, 710021 (China)

E-mail: xiaoxuliu@sust.edu.cn

[c] Dr. H. Yi  
Department of Structural Engineering  
University of California San Diego  
La Jolla, CA 92093-0085 (USA)

determines the system's electrochemical performance and production cost. Among them, nanostructured molybdenum trioxide ( $\text{MoO}_3$ )-based cathode materials have garnered much interest from researchers. This is because the metal cations or hydrogen ions are easily reversibly intercalated in  $\text{MoO}_3$ . The reaction has a more considerable free energy of formation and relatively higher stability. In recent years,  $\text{MoO}_3$ -based electrodes have also been widely investigated as rechargeable ion battery anodes.<sup>[9a,11]</sup> The  $\text{MoO}_3$ -based cathode energy storage mechanism is based on intercalation reactions, and the  $\text{MoO}_3$ -based anode based on conversion reactions has more significant volume expansion and slower reaction kinetics during cycling.<sup>[12]</sup> Therefore, it has more advantages as a cathode material for rechargeable ion batteries. In this review, we comprehensively summarize the application of  $\text{MoO}_3$  as the cathode in rechargeable ion batteries based on intercalation reaction and the standard preparation and modification strategies of the  $\text{MoO}_3$ -based cathode. The energy storage mechanism, existing problems, and optimization strategies of  $\text{MoO}_3$  in non-aqueous lithium-ion batteries (LIBs), magnesium-ion batteries (MIBs), calcium-ion batteries (CIBs), aqueous zinc-ion batteries (ZIBs), hydrogen-ion batteries (HIBs), and aluminum-ion batteries (AIBs) were studied. Finally, molybdenum trioxide cathode's challenges and future development in electrochemical energy storage prospect.

## 2. Crystal Structures and Synthesis of Molybdenum Trioxide

### 2.1. Typical crystal structures

The typical crystal structures of molybdenum trioxide ( $\text{MoO}_3$ ) include thermodynamically stable orthorhombic  $\text{MoO}_3$  ( $\alpha\text{-MoO}_3$ ), metastable monoclinic  $\text{MoO}_3$  ( $\beta\text{-MoO}_3$ ) and hexagonal  $\text{MoO}_3$  ( $h\text{-MoO}_3$ ).  $\text{MoO}_3$  of all three crystal structures is composed of twisted distorted  $\text{MoO}_6$  octahedra (Figure 1a–c). There are three types of oxygen atoms,  $O_t$ ,  $O_a$ , and  $O_s$ , in the  $\text{MoO}_6$  octahedron.  $O_t$  is the terminal oxygen atom,  $O_a$  is the asymmetric oxygen atom, and  $O_s$  is the symmetric bridging oxygen atom (Figure 1a). The  $O_t$  only bonds to one Mo atom with an average bond length of 1.67 Å, the  $O_a$  bonds to two Mo atoms with bond lengths of 1.74 Å and 2.25 Å, and the  $O_s$  bonds to three Mo atoms with two symmetrical horizontal bond lengths of 1.95 Å and one vertical bond length of 2.33 Å.



Xiaoxu Liu received the Ph.D. in the College of Materials Science and Engineering, from the Harbin University of Science and Technology (2012). He was a research fellow in the School of Physical and Mathematical Sciences at the Nanyang Technological University. He is a Professor in the Shaanxi University of Science and Technology. His current research interests mainly focus on the design, fabrication, and application of carbon-based composite.

The crystal structure of the thermodynamically stable phase  $\alpha\text{-MoO}_3$  was first determined in the 1931 s.<sup>[13]</sup> The  $\alpha\text{-MoO}_3$  is composed of two layers of  $\text{MoO}_6$  octahedra with standard edges. Each layer of  $\text{MoO}_6$  octahedra shares corners along [001] and [100] and shares edges along [010]. Each anisotropic bilayer  $\text{MoO}_6$  octahedron is stacked by van der Waals force interactions. The crystal constants of  $\alpha\text{-MoO}_3$  are  $a = 3.962$  Å,  $b = 13.855$  Å, and  $c = 3.697$  Å. The metastable  $\beta\text{-MoO}_3$  has a  $\text{ReO}_3$ -type structure. The  $\text{MoO}_6$  octahedron that constitutes  $\beta\text{-MoO}_3$  shares the corners of the three-dimensional structure to form a monoclinic phase. Different from  $\alpha\text{-MoO}_3$ , the  $\text{MoO}_6$  octahedra that include  $\beta\text{-MoO}_3$  share corner points on the three-dimensional structure, resulting in  $\beta\text{-MoO}_3$  not connected by double layers and not layered (Figure 1b). The metastable  $h\text{-MoO}_3$  has a hexagonal structure. The  $h\text{-MoO}_3$  has a one-dimensional tunnel along the c-axis surrounded by 12  $\text{MoO}_6$  octahedra with a diameter of about 3.0 Å. The  $\text{MoO}_6$  octahedra in  $h\text{-MoO}_3$  share corners along the a and b directions and connecting edges along the c direction (as shown in Figure 1c).

There is a strong correlation between ion storage behavior and crystal structure in  $\text{MoO}_3$ . In the typical crystal structure, the thermodynamically stable  $\alpha\text{-MoO}_3$  is a promising high specific capacity cathode material. The  $\alpha\text{-MoO}_3$  interlayer by van der Waals force, layer by solid covalent bond connected structure, is especially suitable for cation intercalation reaction in aqueous and non-aqueous electrolytes. It has been widely studied in rechargeable ion batteries, while metastable  $\beta\text{-MoO}_3$  and  $h\text{-MoO}_3$  have limited research as cathode materials for rechargeable ion batteries.<sup>[14]</sup> In non-aqueous LIBs applications, compared with the layered structure of  $\alpha\text{-MoO}_3$  that promotes  $\text{Li}^+$  reaction kinetics and facilitates  $\text{Li}^+$  storage,  $h\text{-MoO}_3$  has a hexagonal structure with a one-dimensional tunnel along the c-axis. Although it allows  $\text{Li}^+$  to intercalate and diffuse, it has an initial capacity of more than 400 mA h g<sup>-1</sup> corresponding to  $\text{Li}^+$  storage of 2.2 Li/Mo.<sup>[15]</sup> However, rapid conversion to an amorphous structure after several electrochemical cycles is detrimental to  $\text{Li}^+$  storage.<sup>[16]</sup> In the aqueous AIBs,  $h\text{-MoO}_3$  with tunnel structure is more advantageous. In the report of Hsu et al.,<sup>[17]</sup> the SEM images of  $\text{MoO}_3$  with different crystal structures are shown in Figure 1(d–f). The  $\alpha\text{-MoO}_3$  is a one-dimensional nanobelt with a width of 200 nm and a length of several microns,  $\beta\text{-MoO}_3$  is a nanoparticle with a diameter of about 100–200 nm, and  $h\text{-MoO}_3$  is a hexagonal cylinder with a relatively large size of several microns. In-situ EXAFS shows the evolution of  $\text{MoO}_3$  octahedron structure in  $\text{MoO}_3$  with different crystal structures. Stability of  $\text{MoO}_3$  with other crystal structures



Qiang Zhang Harbin Normal University, associate professor, Ph.D., master supervisor, graduated from the Harbin University of Science and Technology School in 2019, mainly engaged in the electromagnetic and energy storage properties of hyperbolic metamaterials.

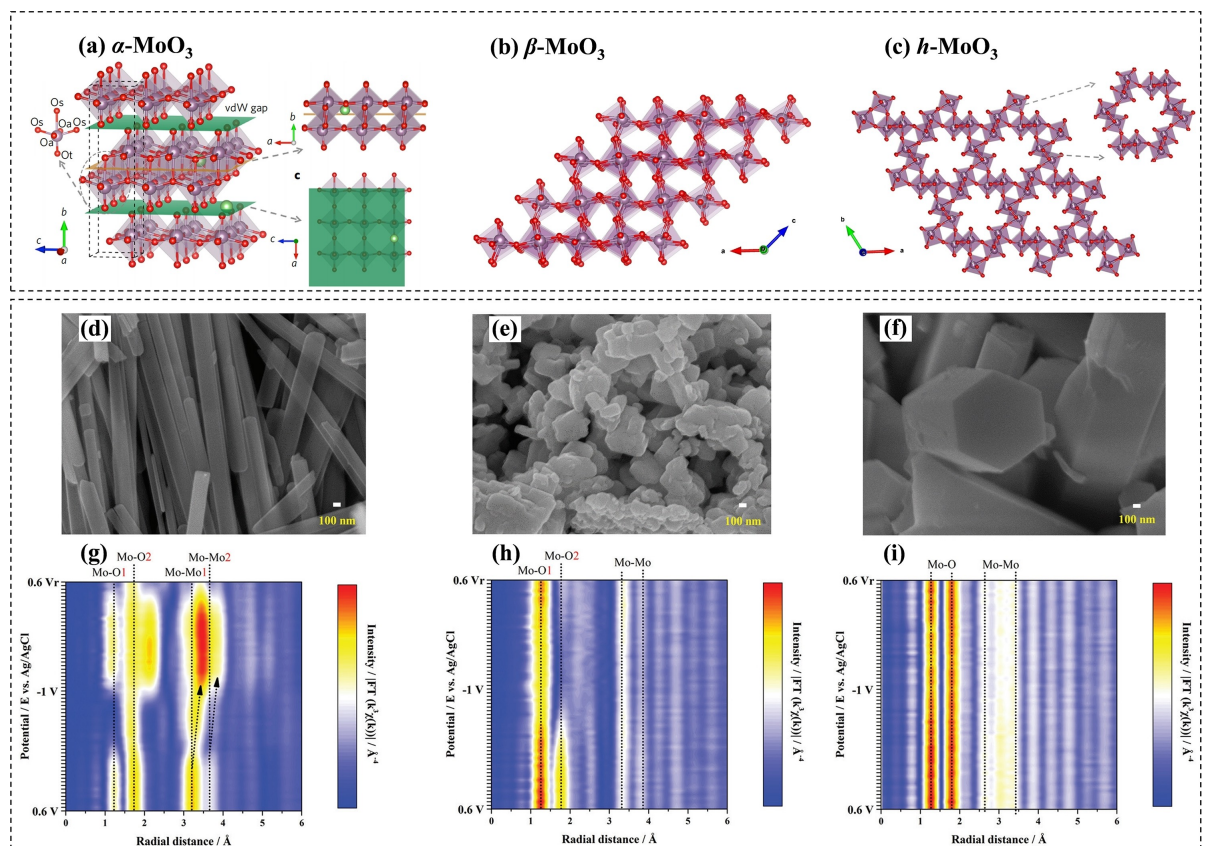


**Figure 1.** a) crystal structure of  $\alpha$ -MoO<sub>3</sub>. Reproduced with permission from Ref. [18]. Copyright (2016) Springer Nature. b) crystal structure of  $\beta$ -MoO<sub>3</sub>. c) crystal structure of  $h$ -MoO<sub>3</sub>. d) SEM images of  $\alpha$ -MoO<sub>3</sub>, e)  $\beta$ -MoO<sub>3</sub> and f)  $h$ -MoO<sub>3</sub>. g) EXAFS spectra of  $\alpha$ -MoO<sub>3</sub>, h)  $\beta$ -MoO<sub>3</sub>, and i)  $h$ -MoO<sub>3</sub>. Reproduced with permission from Ref. [17]. Copyright (2022) Royal Society of Chemistry.

in intercalation and deintercalation of Al<sup>3+</sup> determined by R-space  $|FTk\chi(k)|$  EXAFS test results. The peak intensities of Mo–O1 and Mo–O2 bonds in  $\alpha$ -MoO<sub>3</sub> and  $\beta$ -MoO<sub>3</sub> have significantly been affected during the deintercalation of Al<sup>3+</sup>. There Mo–Mo bonds of  $\alpha$ -MoO<sub>3</sub> merge into a straight line during the intercalation-deintercalation of Al<sup>3+</sup> ions, indicating that the degree of disorder around Mo atoms is increasing. There  $\alpha$ -MoO<sub>3</sub> and  $\beta$ -MoO<sub>3</sub> are prone to crystal structure distortion during the deintercalation of Al<sup>3+</sup>, but  $h$ -MoO<sub>3</sub> is less affected and relatively stable (Figure 1g–i), showing better Al<sup>3+</sup> storage performance in aqueous AlIBs.

## 2.2. Synthesis methods

The standard synthesis methods of MoO<sub>3</sub> include the hydrothermal method, electrochemical deposition, sol-gel method, liquid exfoliation method, physical vapor deposition method (PVD), and chemical vapor deposition method (CVD) and their improved methods. Different synthesis conditions greatly influence the crystal structure and morphology of MoO<sub>3</sub>. The reaction medium is the liquid phase or vapor phase, and the preparation method is divided into liquid phase synthesis and gas phase synthesis, as shown in Figure 2. And the advantages

and limitations of different preparation methods are shown in Table 1.

### 2.2.1. Liquid-phase Synthesis

The hydrothermal method is one of the most common methods for preparing nanostructured MoO<sub>3</sub>. The hydrothermal method's general preparation strategy is to use molybdate as the molybdenum source in a concentrated acid medium and react in a hydrothermal reactor at a temperature of 80–220 °C. Yao et al.<sup>[19]</sup> prepared the ultra-long  $\alpha$ -MoO<sub>3</sub> nanobelts with a length of 200 μm by hydrothermal reaction at 220 °C for 168 h. Remarkably, the aspect ratio of the nanobelts increases linearly with the hydrothermal reaction time, and the nanobelts prepared at 220 °C are substantially longer than that of the  $\alpha$ -MoO<sub>3</sub> nanobelts prepared at 180 °C. In the preparation of MoO<sub>3</sub> by hydrothermal method, not only does the reaction temperature and time have a significant influence on the nanostructured  $\alpha$ -MoO<sub>3</sub>, but also the selection of hydrothermal reaction solvent and the addition of surfactant have a tremendous influence on the atomic structure and morphology of  $\alpha$ -MoO<sub>3</sub>. Changing the hydrothermal reaction solvent, Wu et al.<sup>[20]</sup> further optimized by replacing the deionized water in the hydrothermal reaction precursor solution preparation

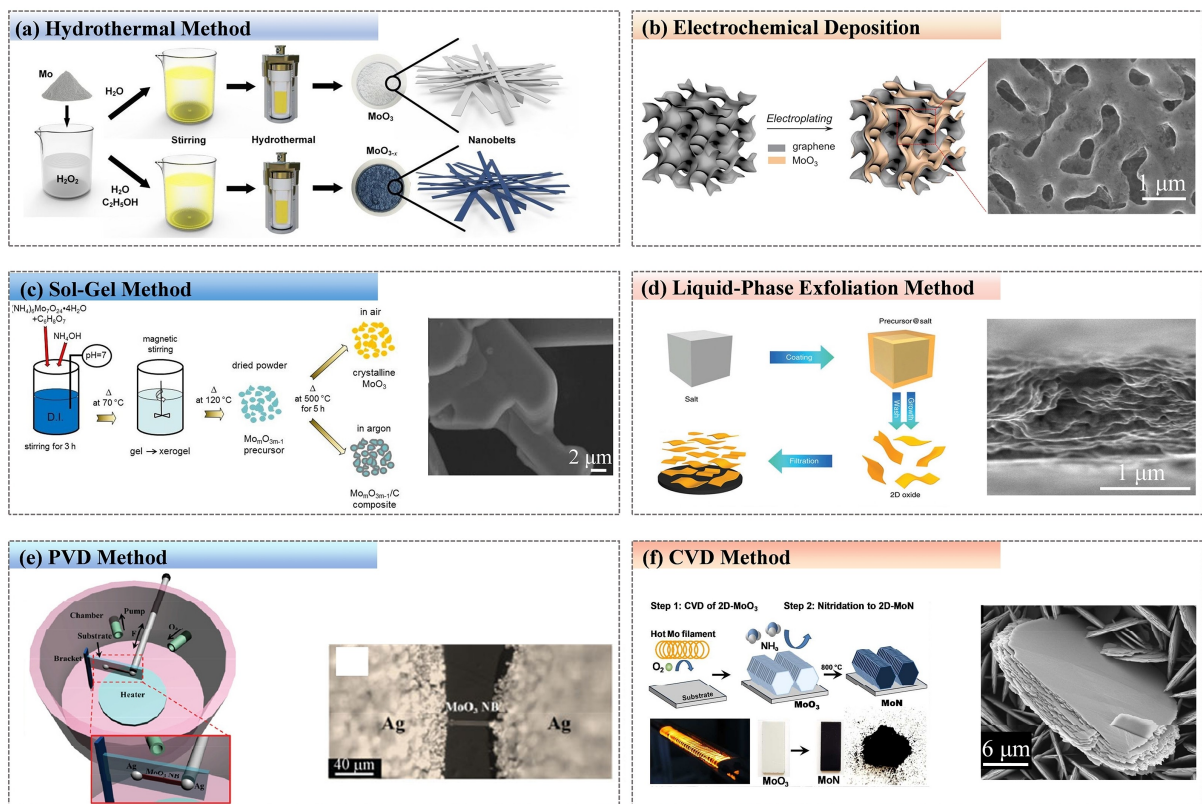


**Figure 2.** a) Hydrothermal method. Reproduced with permission from Ref. [20]. Copyright (2019) Royal Society of Chemistry. b) Electrochemical deposition. Reproduced with permission from Ref. [22]. Copyright (2018) Elsevier. c) Sol-gel method. Reproduced with permission from Ref. [27]. Copyright (2020) Multidisciplinary Digital Publishing Institute. d) Liquid-phase exfoliation method. Reproduced with permission from Ref. [32]. Copyright (2016) Springer Nature. e) PVD method. Reproduced with permission from Ref. [34]. Copyright (2013) Springer Nature. f) CVD method. Reproduced with permission from Ref. [25]. Copyright (2015) WILEY-VCH.

**Table 1.** The advantages and limitations of different preparation methods of MoO<sub>3</sub>.

Methods	Reaction medium	Molybdenum source	Reaction temperature [°C]	Reaction period	Structure	Advantage	Limitation	Reference
Hydrothermal method	Concentrated acid medium	Molybdate	80–220 °C	3–168 h	Nanobelt	High purity and good crystallinity	High requirements for production equipment	[19]
Electrochemical deposition	(NH <sub>4</sub> ) <sub>6</sub> Mo <sub>24</sub> aqueous solution	Electrodeposition bath	Room temperature	54 s (each cycle)	Nano-coating	Low cost and high efficiency	Deposition on conductive substrates	[23]
Sol-gel method	H <sub>2</sub> O	(NH <sub>4</sub> ) <sub>6</sub> Mo <sub>24</sub> ·4H <sub>2</sub> O	Room temperature	3 h	Particle	variety of nanostructure	need subsequent annealing process	[26]
Liquid exfoliation method	IPA/H <sub>2</sub> O	Bulk MoO <sub>3</sub>	Room temperature	more than 10 h	2D nano-sheet	Unique 2D nanostructures	precursors stripping time is long	[31]
PVD method	Air/ar	MoO <sub>3</sub> powder	600 °C	4 h	Nanobelt	high crystallinity	usually requires high energy	[34]
CVD method	Ar with O <sub>2</sub> 7%	Mo wire	300 °C	2.5 h	Nanoparticle	requires less energy	Local deposition is not as convenient as PVD.	[35]

process with a mixed solution of ethanol, and deionized water can prepare oxygen-deficient  $\alpha$ -MoO<sub>2.4</sub>, as shown in Figure 2(a). Cui et al.<sup>[21]</sup> Using different surfactants such as chitosan (CS) and cetyltrimethylammonium bromide (CTAB) can guide the formation of  $\alpha$ -MoO<sub>3</sub> microspheres, microstrips, and nanorods with different morphologies. Microwaves can assist in further improvement of the hydrothermal reaction to shorten the hydrothermal reaction time. Zakharova et al.<sup>[16]</sup> investigated prepared a more significant aspect ratio of  $\alpha$ -MoO<sub>3</sub> nanobelts and  $h$ -MoO<sub>3</sub> microrods by microwave hydrothermal reaction for only 20 minutes. The hydrothermal method has the advantages of a simple process and broad applicability. It can prepare nanostructured MoO<sub>3</sub> with high purity and good crystallinity without sintering. But the phenomenon in the reaction process is challenging to observe, and the reaction steps of high temperature and high pressure have high requirements for production equipment.

Electrochemical deposition is a simple and low-cost preparation method that can control the thickness and morphology of the product at room temperature. When modifying MoO<sub>3</sub> to composite with conductive materials, MoO<sub>3</sub> can be uniformly deposited on carbon, metal, or polymer substrates by electro-deposition. Han et al.<sup>[22]</sup> prepared porous MoO<sub>3</sub>/graphene nanocomposites by applying a pulse voltage on the nanoporous graphene cathode through a three-electrode system (Figure 2b). The three-electrode system consists of Pt and Ag/AgCl as the counter and reference electrodes. Similarly, Spencer et al.<sup>[23]</sup> achieved double-sided deposition of MoO<sub>3</sub> on carbon nanotubes by electrochemical deposition and synthesized a three-dimensional LIBs cathode material with a high active material load. Moreover, Wu et al.<sup>[24]</sup> were able to introduce adjustable oxygen vacancies in MoO<sub>3</sub> by electrochemical deposition. Electrochemical deposition can also achieve MoO<sub>3</sub> coating on other electrode materials. Wang et al.<sup>[25]</sup> prepared MoO<sub>3</sub> shell on TiO<sub>2</sub> nanowire arrays by electrochemical deposition. The synthesized composite nanowire core-shell arrays have a surface capacity comparable to commercial electrodes. The electrochemical deposition has the advantages of low synthesis cost, high efficiency, and extensibility, but it is usually limited to deposition on conductive substrates.

Preparation of MoO<sub>3</sub> by sol-gel method occurs at a relatively low temperature, the use of precursor molecules into nano-clusters (sol) and then generate nano-network (gel), and then by annealing to prepare phase and stoichiometric ratio controllable preparation process. The precursor used in the synthesis, the selected solvent, and the subsequent annealing temperature significantly affect the morphology and structure of MoO<sub>3</sub>. Hashem et al.<sup>[26]</sup> reported rich in oxygen-containing defects, MoO<sub>3</sub> nanoparticles with a thickness of 200 nm were prepared by the sol-gel method using ammonium molybdate as a molybdenum source and citric acid. Furthermore, to optimize the Li<sup>+</sup> storage performance of MoO<sub>3</sub>, Hashem et al.<sup>[27]</sup> prepared  $\alpha$ -MoO<sub>3</sub> and amorphous carbon-encapsulated Mo<sub>m</sub>O<sub>3m-1</sub>/carbon nanocomposites ( $m \approx 5$ ) by heating citrate-gel precursors in an oxygen and argon atmosphere, respectively. The synthesis process and the SEM morphology are the stacked layers of pure MoO<sub>3</sub> are shown in Figure 2(c). Kim et al.<sup>[28]</sup> the

combined sol-gel method with the Joule heating method prepares a unique structure of lamellar micron flower-like MoO<sub>3</sub>. The sol-gel way can synthesize a variety of nanostructured MoO<sub>3</sub> at low temperatures, but it usually needs to be combined with a subsequent annealing process.

The liquid-phase exfoliation method is efficient and environmentally friendly for preparing two-dimensional MoO<sub>3</sub> nanosheets with a high aspect ratio. Initially, Hanlon et al.<sup>[29]</sup> demonstrated that two-dimensional MoO<sub>3</sub> nanosheets can be prepared by the liquid-phase exfoliation method of MoO<sub>3</sub> powder through a series of common dissolvents. In the choice of dissolvent, Zhang et al.<sup>[30]</sup> used isopropanol (IPA) and deionized water mixed dissolvent as dispersion medium to prepare MoO<sub>3</sub> nanosheets with a high aspect ratio of 80–800 and thickness of 2–6 nm by ultrasonic stripping of bulk  $\alpha$ -MoO<sub>3</sub> powder for 10 h. They use IPA, and deionized water as the mixed dissolvent can obtain higher concentration nanosheets. To further optimize the liquid-phase exfoliation method to be more environmentally friendly and to prepare modified MoO<sub>3</sub> nanosheets, Etman et al.<sup>[31]</sup> prepared oxygen-deficient MoO<sub>3-x</sub> nanosheets by liquid-phase exfoliation using commercially available MoO<sub>2</sub> and MoO<sub>3</sub> as raw materials with only water as the dispersion medium. Xiao et al.<sup>[32]</sup> used water-soluble salt crystals as growth templates to prepare  $h$ -MoO<sub>3</sub> two-dimensional nanosheets with large lateral sizes up to 100  $\mu\text{m}$  based on the liquid-phase exfoliation method, showing high pseudo-capacitance performance. The synthesis process is shown in Figure 2(d).

## 2.2.2. vapor-phase synthesis

The preparation of MoO<sub>3</sub> by vapor deposition is achieved by evaporating and condensing the source material onto the target substrate, generally divided into the Physical vapor deposition method (PVD) and chemical vapor deposition method (CVD). The difference between the two is that the PVD method is deposited on the surface of the substrate by physical methods such as evaporation and sputtering. In contrast, the CVD method is a process in which solid deposits are formed by the reaction of gaseous or vapor-state substances on the gas phase or gas-solid interface. In the PVD method, Sun et al.<sup>[33]</sup> by direct current magnetron sputtering of the PVD method, the metal molybdenum as the target, the preparation of oxygen-containing defects in the vertical arrangement of MoO<sub>3</sub> nanosheet arrays, combined with solid electrolyte, lithium metal anode assembled into all-solid-state batteries, the MoO<sub>3</sub> with 3D structure as cathode material in solid-state battery application advantages. Wen et al.<sup>[34]</sup> synthesized single crystal  $\alpha$ -MoO<sub>3</sub> nanobelts with different morphologies by PVD method in air and argon atmospheres using MoO<sub>3</sub> as a molybdenum source. The nanobelts synthesized in argon atmosphere are broader and thicker than those synthesized in air atmosphere. The synthesis process is depicted in Figure 2(e), and the Figure 2(e) optical image on the right side is thinner and narrower nanobelts synthesized in an air atmosphere. Although the PVD method usually requires high energy, its products

have the advantages of high crystallinity, controllable stoichiometric ratio, and controllable morphology. Compared with the PVD method, the CVD method requires much less energy to synthesize MoO<sub>3</sub>. Riley et al.<sup>[35]</sup> prepared uniform MoO<sub>3</sub> nanoparticles by hot-wire CVD method using a single molybdenum wire with a diameter of 0.5 mm as a molybdenum source. Joshi et al.<sup>[25]</sup> preparation of a single crystal MoO<sub>3</sub> two-dimensional layer by hot-wire CVD method shown in the SEM image of Figure 2(f), the phase transition MoO<sub>3</sub> nitride was prepared by further annealing MoO<sub>3</sub> nanosheets in ammonia. In the preparation process, MoO<sub>3</sub> with different stoichiometric ratios can be prepared using the filament power and oxygen partial pressure without introducing an additional reducing agent. The synthesis process is shown in Figure 2(f).

### 3. Electrochemical Energy Storage Application of Molybdenum Trioxide-based Cathode

Among the typical crystal structures of MoO<sub>3</sub>, the  $\alpha$ -MoO<sub>3</sub> is the most widely studied as cathode material for rechargeable ion batteries. This is because the unique layered structure of  $\alpha$ -MoO<sub>3</sub> is very favorable for ion insertion-extraction during

intercalation reaction. To date, MoO<sub>3</sub>-based cathodes have not only been first applied in non-aqueous LIBs but also attracted significant attention in emerging energy storage devices. MoO<sub>3</sub>-based cathodes are explored as cathode materials for emerging energy storage devices, including non-aqueous MIBs, non-aqueous ZIBs, aqueous ZIBs, aqueous HIBs, and aqueous AlBs. Metastable  $h$ -MoO<sub>3</sub> has many reports in aqueous AlBs, and the investigation on  $\beta$ -MoO<sub>3</sub> as a cathode material for rechargeable ion batteries is limited. Figure 3 summarizes the research process of MoO<sub>3</sub> as a cathode in rechargeable ion batteries and the galvanostatic charge-discharge curves in different systems during the cycle process. The energy storage mechanism of MoO<sub>3</sub>-based cathodes in different systems is other. The left side of the middle illustration in Figure 3 is the energy storage mechanism of MoO<sub>3</sub> in HIB, and the right side is in LIB. In the past, although many review articles on MoO<sub>3</sub>-based electrode materials have been reported,<sup>[36]</sup> there has been no comprehensive investigation on the intercalation reaction mechanism of MoO<sub>3</sub> as a cathode for LIBs and emerging energy storage devices. This section will discuss the energy storage mechanism, advantages, and problems of MoO<sub>3</sub> as a cathode in non-aqueous and aqueous rechargeable ion battery systems.

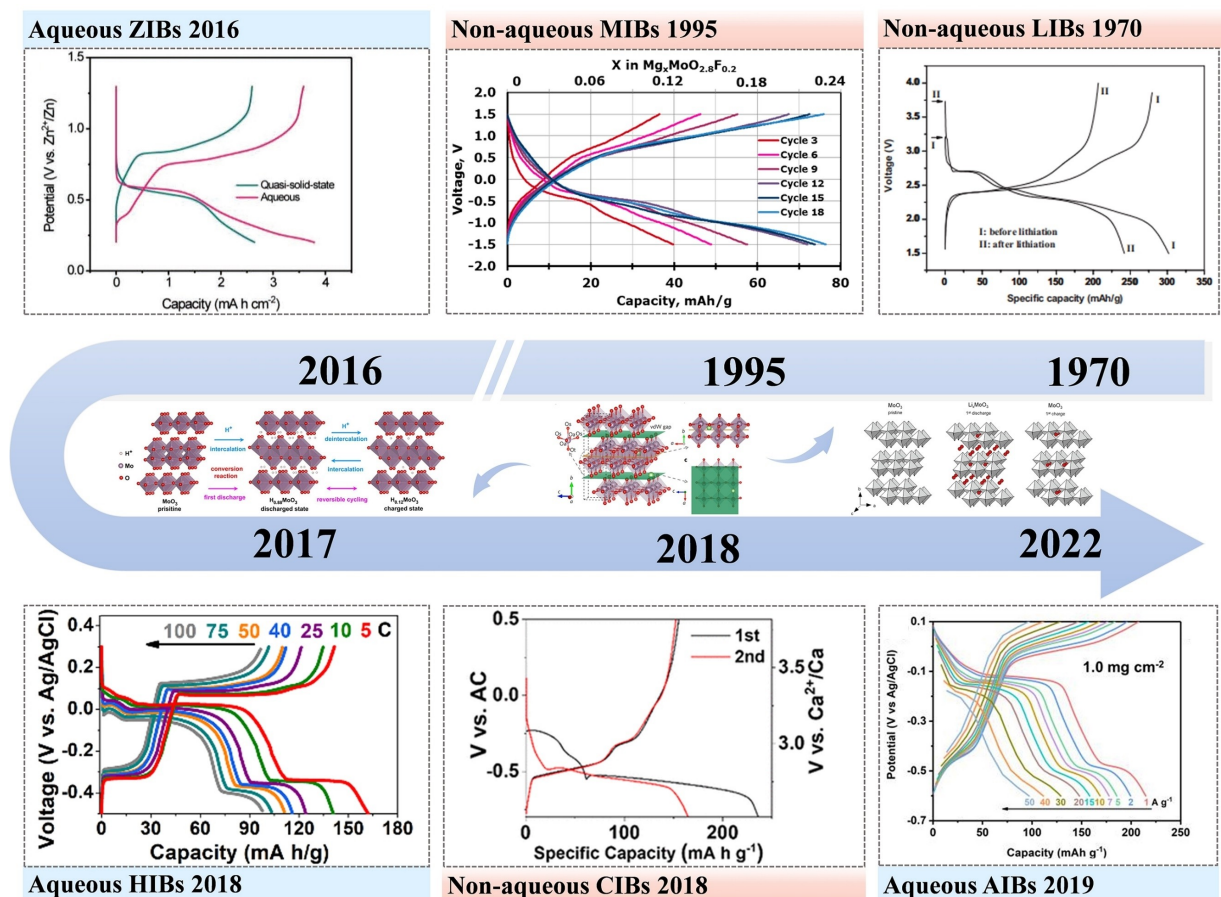


Figure 3. A brief history of the development of MoO<sub>3</sub>-based cathodes in rechargeable ion batteries.<sup>[9b,18,37]</sup> (LIB: lithium-ion battery; MIB: magnesium-ion battery; ZIB: zinc-ion battery; HIB: hydrogen-ion battery; CIB: calcium-ion battery; AlB: aluminum-ion battery)

### 3.1. Lithium-ion batteries

Although various cathode and anode materials for LIBs have been developed in the past three decades, the current commercial anode material is mainly graphite, and the cathode materials are  $\text{LiCoO}_2$ ,  $\text{LiNi}_{0.8}\text{Co}_{0.15}\text{Al}_{0.05}\text{O}_2$ ,  $\text{LiNi}_{0.33}\text{Co}_{0.33}\text{Mn}_{0.33}\text{O}_2$ ,  $\text{LiMn}_2\text{O}_4$ , and  $\text{LiFePO}_4$ .<sup>[38]</sup> Constant exploration of electrode materials is critical to meet the future demand for high-energy-density storage. The pseudocapacitive material  $\text{MoO}_3$  has received extensive attention since it was proposed in the 1970s as a cathode material for LIBs. The  $\text{MoO}_3$  cathode has a maximum theoretical energy density of  $930 \text{ Wh kg}^{-1}$  ( $372 \text{ mAh g}^{-1} \times 2.5 \text{ V vs. Li/Li}^+$ ),<sup>[39]</sup> which is significantly higher than the commercial cathode  $\text{LiCoO}_2$  ( $\sim 580 \text{ Wh kg}^{-1}$ ),  $\text{LiNi}_{0.33}\text{Co}_{0.33}\text{Mn}_{0.33}\text{O}_2$  ( $\sim 600 \text{ Wh kg}^{-1}$ ),  $\text{LiMn}_2\text{O}_4$  ( $\sim 400 \text{ Wh kg}^{-1}$ ),  $\text{LiFePO}_4$  ( $\sim 500 \text{ Wh kg}^{-1}$ ). Although  $\text{LiNi}_{0.8}\text{Co}_{0.15}\text{Al}_{0.05}\text{O}_2$  cathode has a high energy density ( $\sim 1000 \text{ Wh kg}^{-1}$ ),<sup>[38]</sup> it has poor cycle stability and safety issues. In detail, the following will explore the advantages, energy storage mechanism, and existing problems of  $\text{MoO}_3$  cathode in LIBs. In this section, we discuss

the benefits, energy storage mechanism, and existing issues of  $\text{MoO}_3$  cathode in LIBs in detail.

The intercalation-deintercalation of lithium ions ( $\text{Li}^+$ ) by the  $\text{MoO}_3$  cathode is a reversible electrochemical reaction based on topological redox, which is different from the reaction mechanism as an anode. Sakaushi et al.<sup>[12b]</sup> investigated  $\text{MoO}_3$  based on the conversion reaction mechanism as an anode material for LIBs, with a high specific capacity of  $1117 \text{ mAh g}^{-1}$ , and the capacity is about three times that of commercial graphite anode ( $372 \text{ mAh g}^{-1}$ ).<sup>[12b]</sup> As an attractive cathode for LIBs,  $\text{MoO}_3$  has a maximum theoretical energy density of  $930 \text{ Wh kg}^{-1}$ <sup>[39]</sup> due to the 2-electron reaction ( $\text{Mo}^{6+}/\text{Mo}^{4+}$ )<sup>[40]</sup> based on intercalation reaction. Compared with  $\text{MoO}_3$  based on conversion reaction as an anode,  $\text{MoO}_3$  based on intercalation reaction as a cathode shows more significant advantages in reaction kinetics and volume strain. Li et al.<sup>[12a]</sup> characterized the lithium storage mechanism of  $\alpha\text{-MoO}_3$  by in-situ TEM (Figure 4a), and clearly described the two reactions of  $\text{Li}^+$  insertion into  $\alpha\text{-MoO}_3$ , intercalation reaction, and conversion reaction. The initial intercalation reaction of  $\alpha\text{-MoO}_3$  forms  $\text{Li}_2\text{MoO}_3$ , and further insertion of  $\text{Li}^+$  forms Mo and  $\text{Li}_2\text{O}$ .

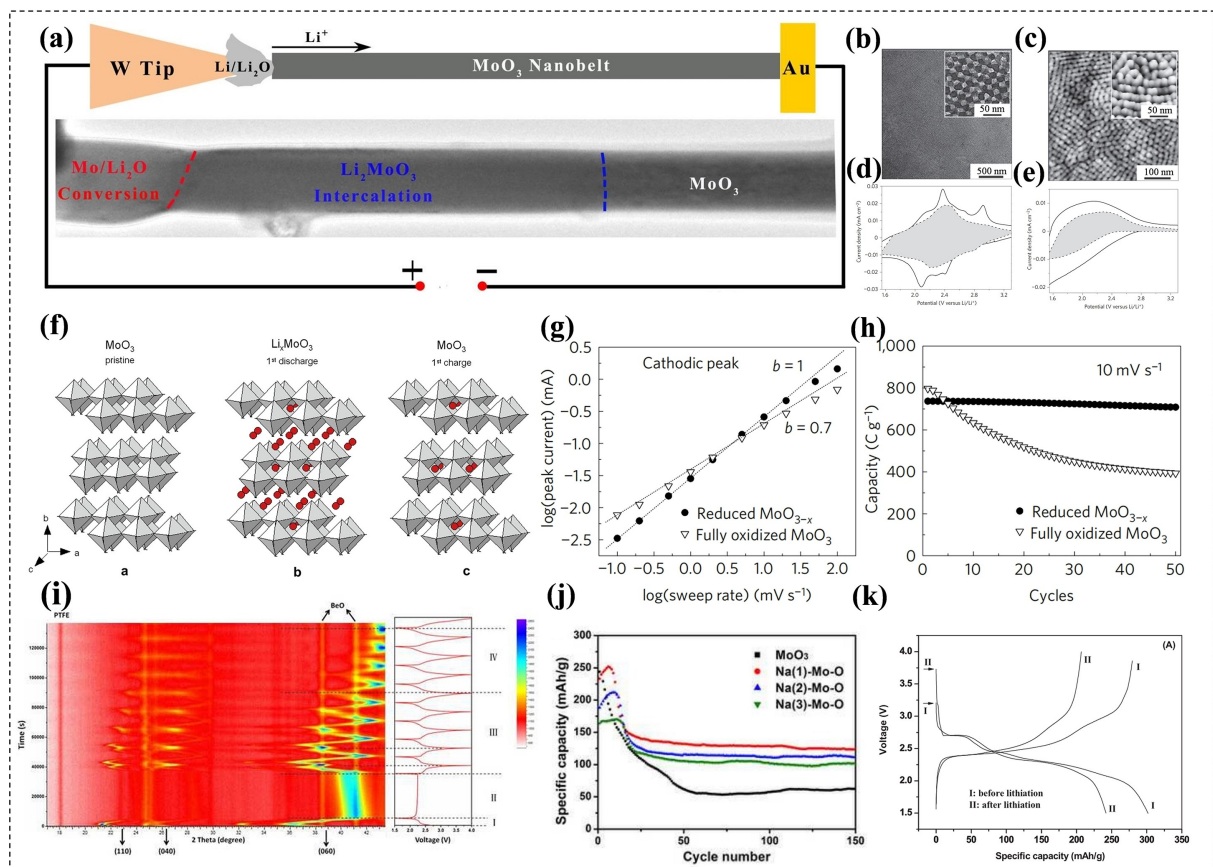
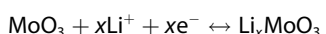


**Figure 4.** a) The lithium storage mechanism of  $\alpha\text{-MoO}_3$  by in-situ TEM. Reproduced with permission from Ref. [12a]. Copyright (2016) Elsevier. b) Morphology of mesoporous  $\alpha\text{-MoO}_3$ . c) Capacitive charge storage contribution for mesoporous  $\alpha\text{-MoO}_3$ . d) Capacitive charge storage contribution for mesoporous amorphous  $\text{MoO}_3$ . Reproduced with permission from Ref. [41]. Copyright (2010) Springer Nature. f) Lithium storage mechanism of  $\alpha\text{-MoO}_3$ . Reproduced with permission from Ref. [45]. Copyright (2008) Elsevier. g) The  $\log(i)$  versus  $\log(v)$  plot of R- $\text{MoO}_{3-x}$  and F- $\text{MoO}_3$ . h) Cycling performance of R- $\text{MoO}_{3-x}$  and F- $\text{MoO}_3$ . Reproduced with permission from Ref. [18]. Copyright (2016) Springer Nature. i) In-situ XRD pattern of Na-Mo-O electrode. j) Cycling performance of Na-Mo-O electrode. Reproduced with permission from Ref. [44]. Copyright (2015) Elsevier. k) The galvanostatic charge curve of the  $\alpha\text{-MoO}_3$  nanobelts before and after lithiation. Reproduced with permission from Ref. [37f]. Copyright (2007) WILEY-VCH.

Comparing the two reaction mechanisms of  $\alpha$ -MoO<sub>3</sub>, the conversion process leads to a huge volume expansion (about 13 times that of the intercalation process) and a slow reaction rate (about 4 times that of the intercalation process). MoO<sub>3</sub> exhibits pseudocapacitance characteristics for charging in seconds as a cathode. Dunn and co-workers studied the pseudocapacitive properties of MoO<sub>3</sub>. Among them, the ordered mesoporous MoO<sub>3</sub> film has a significantly enhanced charge-storage property than the amorphous and non-porous MoO<sub>3</sub> film.<sup>[41]</sup> Sol-gel precursors and evaporation structure-directing agents method prepared the ordered mesoporous MoO<sub>3</sub> film. The morphology of ordered mesoporous MoO<sub>3</sub> film is shown in Figure 4(b and c). The capacitance contribution of ordered mesoporous MoO<sub>3</sub> films is significantly enhanced. The enhanced capacitance contribution is due to the nanocrystalline domain and porous structure of ordered mesoporous MoO<sub>3</sub> (Figure 4d and e). Intercalation pseudocapacitance is another capacitance pseudocapacitance of mesoporous crystalline MoO<sub>3</sub>. Ordered mesoporous MoO<sub>3</sub> films have higher energy density while maintaining high power density. Kim et al.<sup>[18]</sup> enhanced the intercalation pseudocapacitance characteristics of the MoO<sub>3</sub> cathode by introducing oxygen defects into  $\alpha$ -MoO<sub>3</sub>. Compared with the fully oxidized  $\alpha$ -MoO<sub>3</sub>, the oxygen-deficient R-MoO<sub>3-x</sub> significantly improves the charge-storage mechanism based on the Faraday reaction. According to the relationship between the current and the scanning rate: calculation  $b=1$ . The current is completely contributed by the capacitance behavior and is not limited by diffusion. Oxygen-deficient R-MoO<sub>3-x</sub> during cycling reduces capacity loss and significantly improves stability (Figure 4g and h). Although MoO<sub>3</sub> is an attractive lithium intercalation cathode material, the low conductivity and slow reaction kinetics still hinder its widespread use. In the report of Mai et al.,<sup>[37f]</sup> the conductivity of pure MoO<sub>3</sub> and lithiated MoO<sub>3</sub> nanobelts was tested. The pure MoO<sub>3</sub> nanobelts exhibit semiconductor behavior, but the lithiated MoO<sub>3</sub> nanobelts exhibit metal behavior with better conductivity than pure MoO<sub>3</sub>.

To further improve the lithium storage properties of the MoO<sub>3</sub> cathode, it is necessary to explore the intercalation reaction mechanism of MoO<sub>3</sub>.<sup>[18]</sup>



After the intercalation reaction, MoO<sub>3</sub> is converted to Li<sub>x</sub>MoO<sub>3</sub>. The galvanostatic charge-discharge (GCD) curve of the initial cycle is shown in Figure 4(k). Hashem et al.<sup>[42]</sup> observed the insertion of Li<sup>+</sup> into the MoO<sub>3</sub> cathode by chemical lithiation. When the range of  $x < 0.25$ , Li<sub>x</sub>MoO<sub>3</sub> remains the crystal structure of orthorhombic MoO<sub>3</sub>. When the range of  $x > 0.25$ , Li<sub>x</sub>MoO<sub>3</sub> began to enter the lithiated phase gradually. Until the range of  $0.5 \leq x \leq 2$ , a series of structures of Li<sub>x</sub>MoO<sub>3</sub> are similar to Li<sub>2</sub>MoO<sub>3</sub>.  $\alpha$ -MoO<sub>3</sub> has two main Li<sup>+</sup> intercalation sites in the interlayer and intralayer of the double-layer MoO<sub>6</sub> octahedron, respectively (Figure 1a).  $\alpha$ -MoO<sub>3</sub> energy storage is mainly achieved by intercalation in the interlayer site of Li<sup>+</sup>.<sup>[43]</sup> In the initial charge-discharge cycle, the capacity of MoO<sub>3</sub> decays rapidly. The Li<sup>+</sup> intercalated MoO<sub>3</sub> intralayer site cannot

be completely deintercalated, resulting in a rapid capacity decay (Figure 4f). The constant intercalation of Li<sup>+</sup> in the intralayer site induces the phase transition and layer deformation of MoO<sub>3</sub>, so the capacity decays rapidly during the initial cycle process (Figure 4j). Tsumura et al.<sup>[37a]</sup> characterized the changes in the layer spacing of  $\alpha$ -MoO<sub>3</sub> with different crystallinity during the Li<sup>+</sup> intercalation process. The layer spacing of the MoO<sub>3</sub> cathode first increases and then decreases during discharge. Dong et al.<sup>[44]</sup> explained the process of  $\alpha$ -MoO<sub>3</sub> layer spacing first expanding and then shrinking during the discharge process by in-situ XRD characterization (Figure 4i). The distortion of the Mo–O bond on the surface of the  $\alpha$ -MoO<sub>3</sub> interlayer causes layer spacing shrinkage. A large amount of Li<sup>+</sup> intercalation makes the interlayer of  $\alpha$ -MoO<sub>3</sub> have electrostatic interaction. Interestingly, the Li<sup>+</sup> intercalation into  $\alpha$ -MoO<sub>3</sub> during the discharge process leads to a metastable thermodynamic structure. The shrinking layer of  $\alpha$ -MoO<sub>3</sub> in metastable structure will unfold rapidly during the relaxation process (Figure 4i). Through the above mechanism analysis, the cycle stability and conductivity of MoO<sub>3</sub> as the cathode of LIBs still need to be further optimized. The application of the MoO<sub>3</sub> cathode in LIBs is shown in Table 2. To further improve the electrochemical performance of MoO<sub>3</sub> as the cathode for LIBs, various methods have been adopted to modify MoO<sub>3</sub>. The optimized structure stability of MoO<sub>3</sub> is achieved by the pre-intercalation ion method as an interlayer pillar. The accelerated kinetic reaction rate is achieved by introducing oxygen defects in MoO<sub>3</sub>. Combining MoO<sub>3</sub> with conductive materials is an effective way to enhance conductivity and reduce the stress of charge storage. These will be introduced in detail in the fourth chapter.

### 3.2. Magnesium-ion batteries

Rechargeable magnesium ion batteries (MIBs) are one of the “beyond Li-ion batteries” candidates because of the high volume-specific capacity of the Mg anode (Mg: 3800 mAh cm<sup>-3</sup>, Li: 2061 mAh cm<sup>-3</sup>), low reduction potential (-2.37 V vs. SHE), abundant resources (the fifth most abundant element in the earth crust) and the non-deposition of dendrites on the Mg anode. However, one of the biggest problems limiting the practical application of MIBs is the slow diffusion kinetics of Mg ions (Mg<sup>2+</sup>) in the cathode.<sup>[60]</sup> Unlike LIBs, the formation of SEI passive film on the Mg anode in MIBs does not allow the diffusion of Mg<sup>2+</sup>. Therefore, the Mg anode requires complex electrolytes that do not form passivation films. This requires cathode materials compatible with complex electrolytes. In recent years, various cathode materials for non-aqueous MIBs have been proposed. The  $\alpha$ -MoO<sub>3</sub> with the layered crystal structure (Figure 1a) is suitable for Mg<sup>2+</sup> intercalation and has a high theoretical capacity of about 372.3 mAh g<sup>-1</sup> (for 2 electrons, Mo<sup>4+</sup> ↔ Mo<sup>6+</sup>). At a voltage of 2.25 V, there is about 200 mAh g<sup>-1</sup> of Mg<sup>2+</sup> intercalation capacity, corresponding to the energy density of 495 Wh kg<sup>-1</sup> and 2332 Wh cm<sup>-3</sup>. The high energy density of  $\alpha$ -MoO<sub>3</sub> is about six times that of the most advanced Chevrel phase (Mg<sub>x</sub>Mo<sub>6</sub>T<sub>8</sub>, T=S, Se) cathode of MIBs

**Table 2.** Application of  $\text{MoO}_3$ -based cathode in lithium-ion battery.

Cathode	Electrolyte	Potential range [V]	Initial capacity [ $\text{mAh g}^{-1}$ ]	Rate capability [ $\text{mAh g}^{-1}$ ]/current density [ $\text{A g}^{-1}$ ]	Cycling life	Reference
$\text{MoO}_{3-x}$	1 M $\text{LiClO}_4$ in PC	1.5–3.5	153	–	53% after 10000 cycles	[18]
$\alpha\text{-MoO}_{3-x}$	1 M $\text{LiPF}_6$ in EC/DEC	1.5–4	224	50/5	30% after 10000 cycles	[46]
Lithiated $\text{MoO}_3$ nanobelts	1 M $\text{LiPF}_6$ in EC/DMC	1.5–4	240	–	92% after 15 cycles	[37f]
Ammonolyzed $\text{MoO}_3$ nano-belt	1 M $\text{LiPF}_6$ in EC/DMC	1.5–3.5	200	75/2	85% after 350 cycles	[47]
$\alpha\text{-MoO}_3$ nanobelt	1 M $\text{LiPF}_6$ in EC/DMC/DEC	1.5–3.75	264	176/5	65% after 50 cycles	[48]
$\alpha\text{-MoO}_3$ microbelt	1 M $\text{LiPF}_6$ in EC/DEC	1.5–3.5	302	99.4/2	89% after 50 cycles	[49]
$\text{MoO}_3$ nanorod	1 M $\text{LiPF}_6$ in EC/DMC/DEC	1.5–3.5	315	170/2	–	[50]
polyaniline/ $\text{MoO}_3$	1 M $\text{LiPF}_6$ in EC/DEC	1.0–4.2	285.8	–	72% after 20 cycles	[51]
Amorphous $\text{Mo}_5\text{O}_{14}$ -type/C	1 M $\text{LiPF}_6$ in EC/DMC	0.6–3.5	703	155/7	99.2% after 85 cycles	[27]
$\text{MoO}_3/\text{N-CNTs}$	1 M $\text{LiPF}_6$ in EC/DMC	1.5–3.5	350	190/0.3	71% after 85 cycles	[52]
$\text{K}_x\text{MoO}_3@\text{C}$	1 M $\text{LiPF}_6$ in EC/DMC	1.5–3.5	245	118/3	83.9% after 500 cycles	[53]
$\text{MoO}_3/\text{graphene}$	1 M $\text{LiPF}_6$ in EC/DMC	1.5–3.5	291	151/2	59% after 100 cycles	[54]
$\text{MoO}_3\text{-rGO}$	1 M $\text{LiPF}_6$ in EC/DEC	1.5–4	289	43/5	85% after 500 cycles	[55]
$\text{MoO}_3\text{-SWCNTs}$	1 M $\text{LiClO}_4$ in PC	1.5–3.5	195	–	62% after 200 cycles	[56]
$\text{MoO}_3$	1 M $\text{LiPF}_6$ in EC/DMC	1.5–3.25	275	50/20	75% after 20 cycles	[12b]
$\text{MoO}_3$ nanobelt	1 M $\text{LiPF}_6$ in EC/DMC	1.5–4	280	–	86% after 20 cycles	[48]
$\text{MoO}_3/\text{Li}_2\text{MoO}_4$	1 M $\text{LiPF}_6$ in EC/DMC/EMC	2.8–4.3	238	130/2	94.8% after 100 cycles	[57]
$\text{PPy}_x\text{MoO}_3$	1 M $\text{LiPF}_6$ in EC/DMC	1.5–3.95	302	–	72% after 14 cycles	[58]
$(\text{PEG})_x\text{MoO}_3$	1 M $\text{LiPF}_6$ in EC/DMC	1.5–3.5	310	–	50% after 25 cycles	[59]

(Chevrel phases: 120  $\text{mAh g}^{-1}$ ; 1.1 V vs. Mg). In the 1995 s, Spahr et al.<sup>[61]</sup> first reported the reversible  $\text{Mg}^{2+}$  intercalation of the  $\alpha\text{-MoO}_3$  cathode in MIBs. The first discharge-specific capacity of the  $\alpha\text{-MoO}_3$  cathode was measured to be 210  $\text{mAh g}^{-1}$  when using Mg as the counter electrode and 1 M  $\text{Mg}(\text{ClO}_4)_2$ /acetonitrile electrolyte containing 3 mol %  $\text{H}_2\text{O}$ . Unfortunately, the  $\alpha\text{-MoO}_3$  cathode exhibits rapid capacity decay during  $\text{Mg}^{2+}$  storage.

To further understand the mechanism of  $\text{Mg}^{2+}$  insertion and extraction in the  $\alpha\text{-MoO}_3$  cathode, the  $\alpha\text{-MoO}_3$  cathode is further explored in MIBs. Gershinsky et al.<sup>[62]</sup> prepared 100 nm thick  $\alpha\text{-MoO}_3$  film deposited on Pt substrate by electrodeposition. This preparation method eliminates the influence of conductive carbon, binder, and substrate. The  $\alpha\text{-MoO}_3$  cathode exhibits reversible structural changes using 0.1 M  $\text{Mg}(\text{TFSI})_2$ /acetonitrile electrolyte. The  $\text{Mg}^{2+}$  intercalation-deintercalation of  $\alpha\text{-MoO}_3$  cathode occurs two-phase reaction and requires a higher  $\text{Mg}^{2+}$  intercalation overpotential than  $\text{Li}^+$ . The structure of the original and intercalated-deintercalated  $\text{Mg}^{2+}$  of the  $\alpha\text{-MoO}_3$  cathode was characterized as shown in Figure 5(a). The ex-situ XRD spectrum shows that although the diffusion kinetics of the  $\text{Mg}^{2+}$  storage process in the  $\alpha\text{-MoO}_3$  cathode is slow,  $\text{Mg}^{2+}$  can be reversibly intercalated-deintercalated in the  $\alpha\text{-MoO}_3$  cathode. In the study of Tarsame et al.,<sup>[63]</sup> the shape of the  $\alpha\text{-MoO}_3$  cathode was almost unchanged after 300 cycles at a scan rate of 100  $\text{mVs}^{-1}$ . This result proves that  $\alpha\text{-MoO}_3$  can be used as a cathode for stable  $\text{Mg}^{2+}$  storage.

To further optimize the  $\text{Mg}^{2+}$  storage performance of the  $\alpha\text{-MoO}_3$  cathode, Incorvati et al.<sup>[37d]</sup> prepared by fluorine doped  $\alpha\text{-MoO}_3$  ( $\alpha\text{-MoO}_{2.8}\text{F}_{0.2}$ ), and the fluorinated  $\alpha\text{-MoO}_{2.8}\text{F}_{0.2}$  can reduce the electrostatic repulsion of  $\text{Mg}^{2+}$ . Compared with

nonfluorinated  $\alpha\text{-MoO}_3$ , the fluorinated  $\alpha\text{-MoO}_{2.8}\text{F}_{0.2}$  cathode shows a higher specific capacity and capacity retention in MIBs with the electrolyte of 0.2 M  $\text{Mg}(\text{TFSI})_2$  in propylene carbonate (PC). The galvanostatic charge-discharge curve of the fluorinated  $\alpha\text{-MoO}_{2.8}\text{F}_{0.2}$  cathode is shown in Figure 5(b). During the cycle, the  $\text{Mg}^{2+}$  storage capacity of  $\alpha\text{-MoO}_{2.8}\text{F}_{0.2}$  gradually increases and becomes more stable. To reduce the polarization and further improve the stability of  $\text{Mg}^{2+}$  storage of  $\alpha\text{-MoO}_3$  cathode,  $\alpha\text{-MoO}_3$  was co-doped with two ions, such as Wang et al. co-doped  $\alpha\text{-MoO}_3$  (HMoOF) by  $\text{F}^-$  and  $\text{H}^+$ , as shown in Figure 5(d). The  $\text{F}^-$  substitution doping generates molybdenum vacancies in  $\alpha\text{-MoO}_3$  to accelerate the diffusion of  $\text{Mg}^{2+}$  along the *b*-axis. The  $\text{H}^+$  interstitial doping expands the layer spacing of  $\alpha\text{-MoO}_3$  as a pillar of the interlayer structure. This doping method enables  $\alpha\text{-MoO}_3$  to remain stable during the charge and discharge cycles process (Figure 5e and f). Reduce the diffusion barrier of  $\text{Mg}^{2+}$  along the AC plane in the HMoOF cathode, as shown in Figure 5(g and h). The HMoOF cathode has a high reversible specific capacity (241  $\text{mAh g}^{-1}$  at 0.1  $\text{Ag}^{-1}$ ), improved rate performance (137.4  $\text{mAh g}^{-1}$  at 2  $\text{Ag}^{-1}$ ), and long cycle stability (98% capacity retention after 800 cycles at 1  $\text{Ag}^{-1}$ ) in MIBs (Figure 5c and f).

### 3.3. Calcium-ion batteries

Calcium-ion batteries (CIBs) have a lower reduction potential (−2.9 V vs. SHE for  $\text{Ca}/\text{Ca}^{2+}$ ), which is close to that of lithium and lower than that of other multivalent ion batteries. It is one of the most promising “post-lithium-ion batteries” due to its potential high energy density, small polarization, faster ion

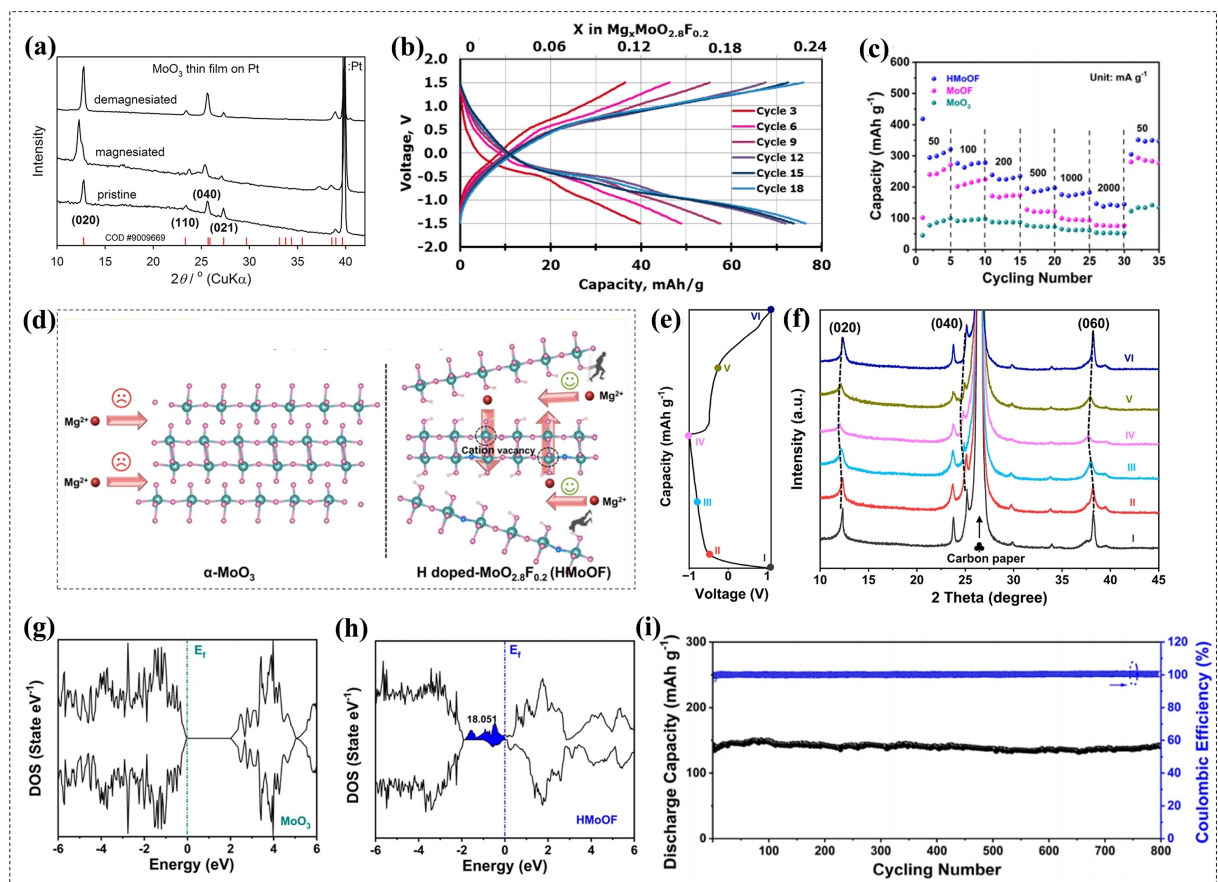


**Figure 5.** a) XRD patterns of pristine and magnesia/demagnetized  $\text{MoO}_3$  electrodes. Reproduced with permission from Ref. [62]. Copyright (2013) American Chemical Society. b) GCD curve of  $\text{MoO}_{2.8}\text{F}_{0.2}$ . Reproduced with permission from Ref. [37d]. Copyright (2016) American Chemical Society. c) The rate capability of  $\text{MoO}_3$ ,  $\text{MoOF}$ , and  $\text{HMoOF}$ . d) Magnesium storage of  $\text{HMoOF}$ . e) GCD curve of  $\text{HMoOF}$ . f) The ex-situ XRD patterns of  $\text{HMoOF}$ . g) Density of states of  $\text{MoO}_3$ . h) Density of states of  $\text{HMoOF}$ . i) Cycling performances of  $\text{HMoOF}$ . Reproduced with permission from Ref. [64]. Copyright (2022) American Chemical Society.

diffusion kinetics, higher safety, and no dendrites. However, compared with LIBs, the exploration of CIBs is still in its infancy. The formation of a surface passivation film on the Ca anode in a conventional non-aqueous electrolyte will make calcium ions ( $\text{Ca}^{2+}$ ) irreversibly stored. Therefore, finding a cathode material compatible with the Ca anode and electrolyte in a non-aqueous electrolyte is essential. The intercalation of  $\text{Ca}^{2+}$  in the cathode material will cause a significant volume change. Therefore, selecting cathode materials with high voltage, high rate performance, and high capacity of  $\text{Ca}^{2+}$  storage is a fundamental challenge for developing CIBs.<sup>[65]</sup>  $\text{MoO}_3$  as an intercalation cathode material has attracted the attention of researchers, and the application of layered  $\alpha\text{-MoO}_3$  cathode to CIBs was first studied in the 2018.<sup>[66]</sup> In the  $\text{MoO}_3$  cathode,  $\beta\text{-MoO}_3$  and  $h\text{-MoO}_3$  are fewer applications. Therefore, this chapter details the feasibility and performance improvement strategy of  $\alpha\text{-MoO}_3$  as a CIB cathode. To illustrate the reversible storage of  $\text{Ca}^{2+}$  by  $\alpha\text{-MoO}_3$  cathode, Tilak et al.<sup>[67]</sup> simulated  $\text{Ca}^{2+}$  intercalation in  $\text{MoO}_3$  interlayer and intralayer by theoretical calculation using density functional theory. It shows that  $\text{Ca}^{2+}$  tends to intercalate into the  $\text{MoO}_3$  interlayer site. Oxygen vacancies in the  $\alpha\text{-MoO}_3$  cathode are not conducive to  $\text{Ca}^{2+}$  intercalation, which was not similar to LIBs. To reveal the energy storage

mechanism of  $\text{Ca}^{2+}$  intercalation in  $\text{MoO}_3$  cathode, Tojo et al.<sup>[66a]</sup> analyze the  $\text{MoO}_3$  cathode in CIBs by ex-situ XRD, XPS, and EDX characterization methods. The  $\text{Ca}^{2+}$  intercalation in the  $\text{MoO}_3$  cathode occurs two-phase reaction during the discharge process. The electrolyte is 0.5 M  $\text{Ca}(\text{TFSI})_2$  dissolved in acetonitrile, charge, and discharge curve, as shown in Figure 6(a). The first discharge and charge-specific capacities of the  $\text{MoO}_3$  cathode are  $186 \text{ mAh g}^{-1}$  and  $116 \text{ mAh g}^{-1}$ , respectively. Most of the irreversible capacity loss is related to the decomposition of the electrolyte. Cabello et al.<sup>[66b]</sup> demonstrated the 0.5 M  $\text{Ca}(\text{TFSI})_2$  in DME as the electrolyte, Ca metal as the anode, and the  $\alpha\text{-MoO}_3$  cathode still retains the layered structure after reversible storage of  $\text{Ca}^{2+}$ . This result proves the application feasibility of  $\alpha\text{-MoO}_3$  cathode in non-aqueous electrolyte CIBs. The slow diffusion of  $\text{Ca}^{2+}$  and the side reaction of electrolyte decomposition during deep discharge are still  $\alpha\text{-MoO}_3$  cathode problems. In addition, there is a conversion reaction competing with the intercalation reaction in the  $\alpha\text{-MoO}_3$  cathode. The conversion reaction of  $\alpha\text{-MoO}_3$  brings about more significant volume expansion and high crystallinity loss. The intercalation and conversion reaction equations in 0.5 M  $\text{Ca}(\text{TFSI})_2$ /DME electrolyte are as follows:

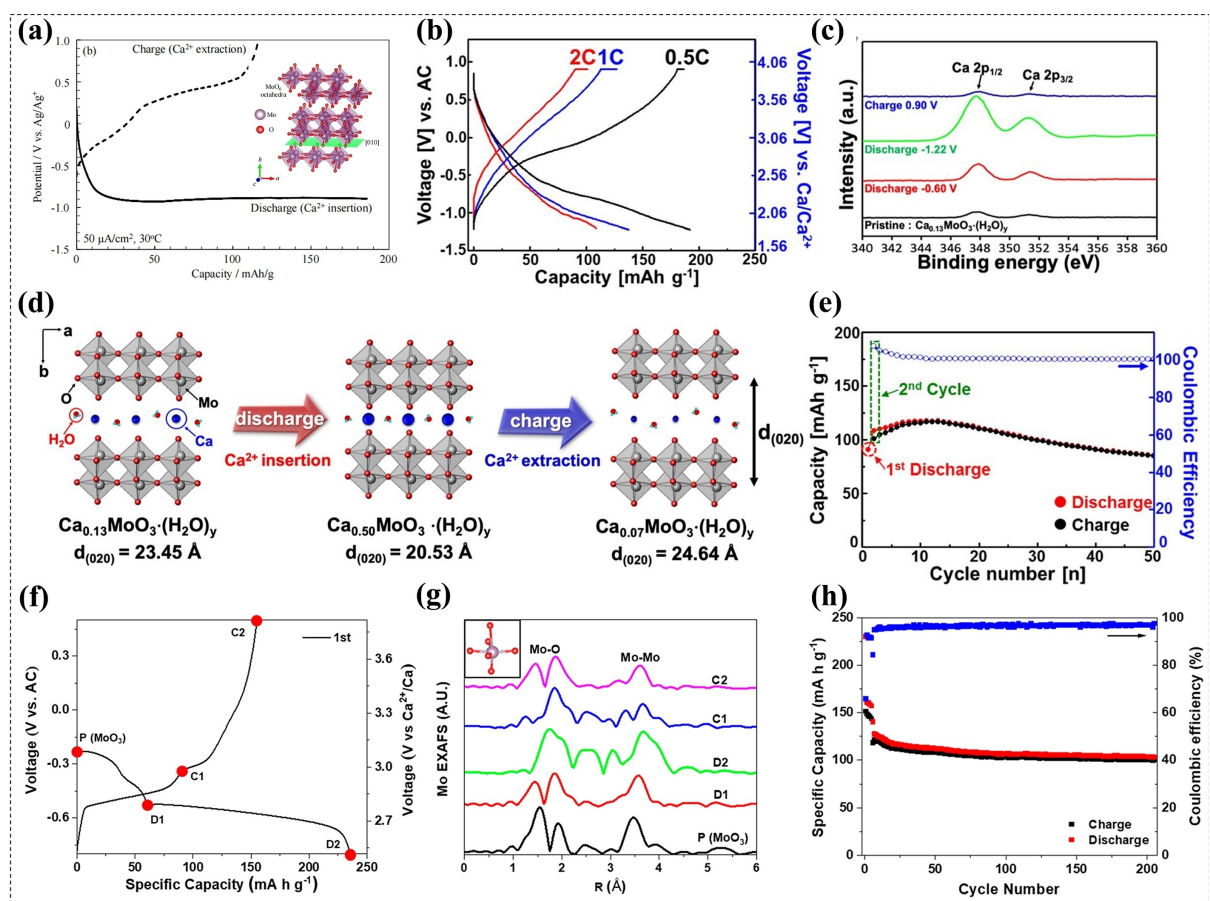
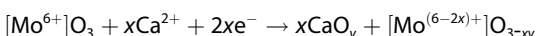
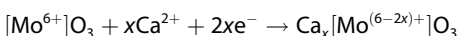


**Figure 6.** a) GCD curves of  $\alpha$ -MoO<sub>3</sub>. Reproduced with permission from Ref. [66a]. Copyright (2018) Elsevier. b) GCD curves of  $\text{Ca}_x\text{MoO}_3\cdot(\text{H}_2\text{O})_y$  at different rates. c) XPS spectra for Ca atoms. d) The schematic of the  $\text{Ca}_x\text{MoO}_3\cdot(\text{H}_2\text{O})_y$ . Structural change upon cycling. e) Cycle performance of  $\text{Ca}_x\text{MoO}_3\cdot(\text{H}_2\text{O})_y$ . Reproduced with permission from Ref. [68]. Copyright (2020) American Chemical Society. f) GCD curve of  $\alpha$ -MoO<sub>3</sub>. g) Mo K-edge EXAFS spectra of  $\alpha$ -MoO<sub>3</sub> at different states of charge-discharge. h) Cycling performance of  $\alpha$ -MoO<sub>3</sub> nanoparticles. Reproduced with permission from Ref. [37e]. Copyright (2022) American Chemical Society.



To improve the performance of  $\alpha$ -MoO<sub>3</sub> cathode, Chae et al.<sup>[68]</sup> prepared  $\text{Ca}_{0.13}\text{MoO}_3\cdot(\text{H}_2\text{O})_{0.41}$  with preferable structural stability and higher ion diffusion kinetics by the cation exchange method. It has an average voltage of about 2.4 V (vs.  $\text{Ca}/\text{Ca}^{2+}$ ) and a reversible discharge capacity of 192 mAh g<sup>-1</sup> under a current density of 86 mAh g<sup>-1</sup>, as shown in Figure 6(b). The XPS spectra proved that  $\text{Ca}_{0.13}\text{MoO}_3\cdot(\text{H}_2\text{O})_{0.41}$  can reversibly insert and extract  $\text{Ca}^{2+}$  during the cycle (Figure 6c). The layer spacing of  $\text{Ca}_{0.13}\text{MoO}_3\cdot(\text{H}_2\text{O})_{0.41}$  increased after  $\text{Ca}^{2+}$  extraction (Figure 6d). After 50 cycles at 2 C, the capacity retention of 94% is shown in Figure 6(e). The stability is significantly improved, but the crystal water in the  $\text{Ca}_{0.13}\text{MoO}_3\cdot(\text{H}_2\text{O})_{0.41}$  structure may reduce the volume energy density and cause side reactions with the electrolyte. Kim et al.<sup>[37e]</sup> prepared  $\alpha$ -MoO<sub>3</sub> nanoparticles to enhance the kinetics of response and reduce the ion diffusion distance, showing significantly improved cycle stability. The  $\alpha$ -MoO<sub>3</sub> nanoparticles can provide 103 mAh g<sup>-1</sup> discharge capacity after 200 cycles at 40 mA g<sup>-1</sup>,

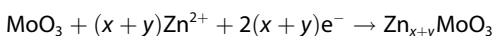
and the coulombic efficiency is stable at about 97.5% (Figure 6h). The galvanostatic charge-discharge curve of the first cycle of  $\alpha$ -MoO<sub>3</sub> nanoparticles is shown in Figure 6(f). The  $\alpha$ -MoO<sub>3</sub> cathode discharged to D<sub>1</sub> and D<sub>2</sub> and charged back to C<sub>1</sub> and C<sub>2</sub> were characterized, and the mechanism of  $\text{Ca}^{2+}$  insertion during the cycle of  $\alpha$ -MoO<sub>3</sub> was analyzed by ex-situ XRD. The  $\alpha$ -MoO<sub>3</sub> nanoparticles had no conversion reactants (Mo, MoO<sub>2</sub>, CaO) during the reaction and maintained the orthorhombic structure. With the intercalation of  $\text{Ca}^{2+}$ , the interlayer spacing of  $\alpha$ -MoO<sub>3</sub> nanoparticles decreased. This is consistent with the research of Chae et al.,<sup>[68]</sup> which is due to the influence of intercalation sites on interlayer connectivity. Through the EXAFS analysis,  $\text{Ca}^{2+}$  is intercalation into the  $\alpha$ -MoO<sub>3</sub>, and the corresponding peaks of Mo–O bonds gradually merge in the discharge process. The initial  $\alpha$ -MoO<sub>3</sub> consists of a distorted MoO<sub>6</sub> octahedron composed of two longer Mo–O bonds and four shorter Mo–O bonds (illustrated in Figure 6g). With  $\text{Ca}^{2+}$  intercalation, the degree of distortion of the MoO<sub>6</sub> octahedron decreases. The MoO<sub>6</sub> octahedron in  $\alpha$ -MoO<sub>3</sub> becomes more symmetrical during the discharge process. The charging process is similar to the initial structure, indicating that the  $\alpha$ -MoO<sub>3</sub> cathode has good local structural reversibility.

The improvement of  $\text{Ca}^{2+}$  intercalation by preparing  $\alpha\text{-MoO}_3$  nanoparticles is consistent with the theoretical study of Das et al.<sup>[67]</sup> It is predicted that  $\alpha\text{-MoO}_3$  nanoparticles with fewer oxygen defects will further increase the specific capacity, indicating that the  $\text{Ca}^{2+}$  storage mechanism in  $\alpha\text{-MoO}_3$  depends on the size effect.

### 3.4. Aqueous zinc-ion battery

The application of  $\text{MoO}_3$ -based cathode in aqueous rechargeable ion batteries is shown in Table 3. Aqueous ZIBs have attracted widespread attention due to their high safety, ease of preparation, abundant reserves, and low price ( $2 \text{ USD kg}^{-1}$ ) of zinc anodes.<sup>[69]</sup> In addition, the zinc anode has a low redox potential ( $-0.762 \text{ V vs. SHE}$ ) and a high weight-specific capacity ( $820 \text{ mAh g}^{-1}$ ) and volume-specific capacity ( $5855 \text{ mAh cm}^{-3}$ ), showing its large-scale application prospects.<sup>[36e]</sup> ZIBs cathode materials mainly include manganese-based, vanadium-based, Prussian blue analog (PBA)-based and other materials. Although the manganese-based cathode has a lower cost, its low conductivity and inevitable severe manganese dissolution lead to poor rate performance and rapid capacity decay. For vanadium-based cathodes with various forms, large-scale applications are hindered by their toxicity and severe structural deformation during cycling. Although Prussian blue analogs have a high voltage platform, low capacity (less than  $100 \text{ mAh g}^{-1}$ ) limits its practical application. In contrast, in recent years,  $\text{MoO}_3$  with layered structure and tunnel structure

(Figure 1a and c) has emerged as a ZIB cathode. This is because  $\text{MoO}_3$  has a high zinc ion ( $\text{Zn}^{2+}$ ) storage capacity ( $372 \text{ mAh g}^{-1}$ ) and a structure conducive to  $\text{Zn}^{2+}$  storage. This section will discuss the zinc storage mechanism, existing problems, and modification methods of the  $\text{MoO}_3$  cathode in detail. Compared with LIBs, the  $\text{Zn}^{2+}$  storage mechanism of the  $\text{MoO}_3$  cathode is similar to the  $\text{Li}^{+}$  storage mechanism. He et al.<sup>[37b]</sup> studied the electrochemical performance of  $\text{MoO}_3$  cathode in ZIBs with  $2 \text{ M ZnCl}_2$  aqueous solution as electrolyte. The cathode reaction in the assembled  $\text{Zn}/\text{MoO}_3$  ZIB is summarized as follows:



(The first discharge cycle);



(The following charge/discharge cycles)

The intercalation process of  $\text{Zn}^{2+}$  in  $\text{MoO}_3$  is illustrated in Figure 7(a). In the first cycle,  $\text{Zn}^{2+}$  cannot be entirely reversibly extracted from the  $\text{MoO}_3$  cathode. During the subsequent process,  $\text{Zn}^{2+}$  is reversibly intercalated and deintercalated in the  $\text{MoO}_3$  cathode.

However, the problem of the  $\text{MoO}_3$  cathode is the dissolution in an aqueous electrolyte and the slow diffusion of  $\text{Zn}^{2+}$ . These problems lead to severe capacity fading and limited rate performance of the  $\text{MoO}_3$  cathode.

To overcome the problems of  $\text{MoO}_3$  cathode in aqueous ZIBs, replacing the electrolyte strategy with gel electrolyte or

**Table 3.** Application of  $\text{MoO}_3$ -based cathode in aqueous rechargeable ion battery.

Application	Anode//Cathode	Electrolyte	Potential range	Initial capacity	Energy density [ $\text{Wh kg}^{-1}$ ]	Power density [ $\text{kW kg}^{-1}$ ]	Rate: capability [ $\text{mAh g}^{-1}$ ]/current density [ $\text{A g}^{-1}$ ]	Cycling life	Reference
ZIBs	$\text{Zn}/\text{MoO}_3$	PVA/ $\text{ZnCl}_2$ gel	0.2–1.3 V vs. $\text{Zn}/\text{Zn}^{2+}$	344	4.9 $\text{mWh cm}^{-3}$	87.2 $\text{mW cm}^{-3}$	243.1/0.4	70.4% after 400 cycles	[84]
ZIBs	$\text{Zn@MXene}/\text{MoO}_3_{x@\text{MXene}}$	$\text{Zn}(\text{OTf})_2\text{-PVA}$	0.25–1.3 V vs. $\text{Zn}/\text{Zn}^{2+}$	369.8	–	–	110.6/4	62.7% after 2000 cycles	[85]
ZIBs	$\text{Zn}/\text{WP-MoO}_3$	2 M $\text{ZnCl}_2$ aqueous solution	0.2–1.3 V vs. $\text{Zn}/\text{Zn}^{2+}$	356.8	198	0.28	275.9/4.8	83% after 1000 cycles	[86]
ZIBs	$\text{Zn}/\text{P-MoO}_3_{x@\text{Al}_2\text{O}_3}$	PVA/ $\text{ZnCl}_2$ gel electrolyte	0.2–1.3 V vs. $\text{Zn}/\text{Zn}^{2+}$	257.7	240	8.500	146.9/20	69.2% after 100 cycles	[87]
HIBs	$\text{Zn}/\alpha\text{-MoO}_3$	32 M $\text{ZnCl}_2$ + 1 mM $\text{P}_2\text{O}_5$ aqueous electrolyte	0.45–1.3 V vs. $\text{Zn}/\text{Zn}^{2+}$	465	–	–	288/16	98% after 1000 cycles	[88]
HIBs	$\text{MoO}_3/\text{MoO}_3$	8 M $\text{H}_2\text{SO}_4$ aqueous solution	−0.7–1.35 V vs. $\text{Ag}/\text{AgCl}$	188	14.7	12.7	120/100	75% after 1000 cycles	[89]
HIBs	$\text{MoO}_3/\text{graphite}$	6 M $\text{H}_2\text{SO}_4$	−0.45–0.3 V vs. SCE	218	–	–	190/20	75% after 5000 cycles	[90]
HIBs	$\text{MoO}_3/\text{MoO}_3$	1 M $\text{H}_2\text{SO}_4$	−0.5–0.3 V vs. $\text{Ag}/\text{AgCl}$	146	–	–	88/20	67% after 100 cycles	[91]
AlBs	$\text{MoTaO}_x/\text{graphite}$ nanorod	0.5 mol/L $\text{Al}_2(\text{SO}_4)_3$	−0.6–0.2 V vs. $\text{Ag}/\text{AgCl}$	–	–	–	–	83% after 3000 cycles	[83]
AlBs	fully oxidized $\text{MoO}_3$ nanobelts	1 mol/L $\text{AlCl}_3$	−0.6–0.1 V vs. $\text{Ag}/\text{AgCl}$	352	–	–	97/50	19% after 10000 cycles	[37c]

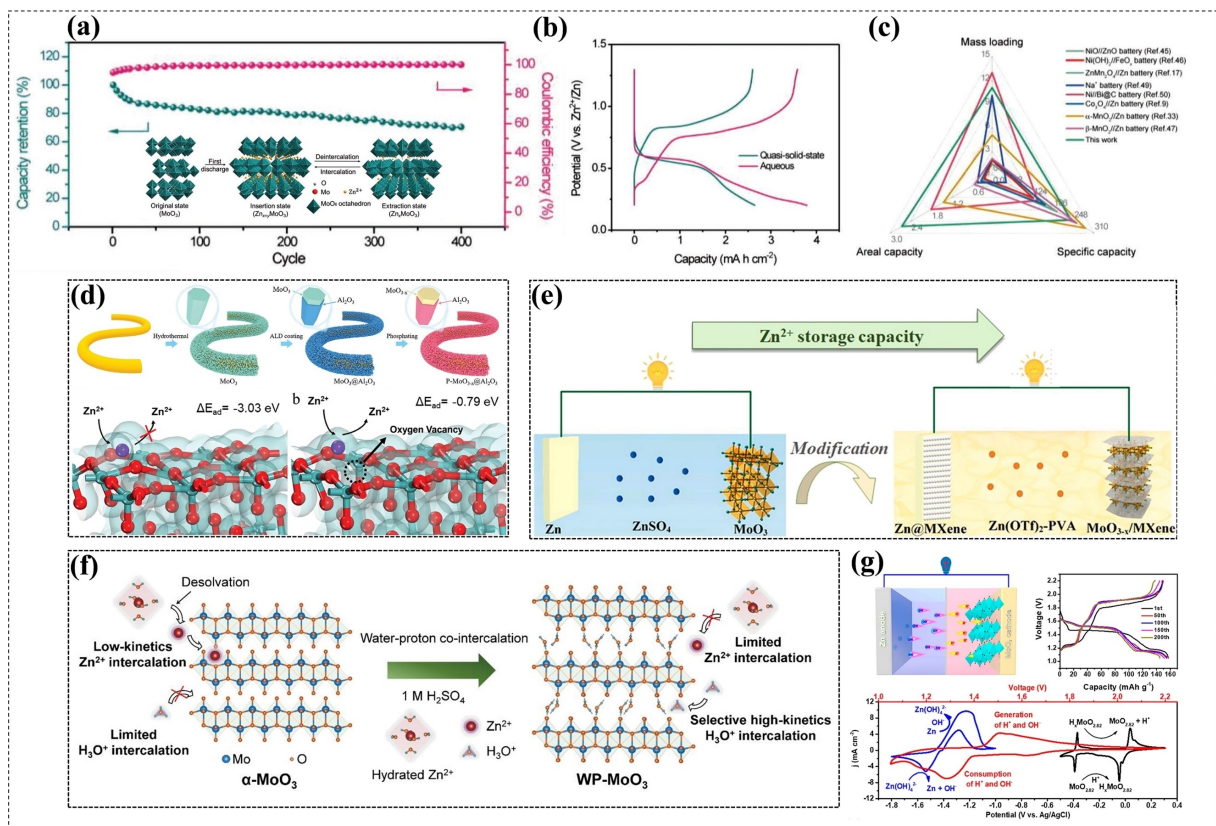


**Figure 7.** a) Cycling performance of the quasi-solid-state Zn//MoO<sub>3</sub> battery. b) The GCD curves of the aqueous and quasi-solid-state Zn//MoO<sub>3</sub> battery. c) A comparison of the quasi-solid-state Zn//MoO<sub>3</sub> battery and some recently reported works. Reproduced with permission from Ref. [37b]. Copyright (2019) WILEY-VCH. d) Schematic illustration of Zn<sup>2+</sup> adsorption-desorption for MoO<sub>3</sub> and MoO<sub>3-x</sub>. Reproduced with permission from Ref. [73]. Copyright (2020) WILEY-VCH. e) Schematics of the initial and modified battery system. Reproduced with permission from Ref. [74]. Copyright (2022) Elsevier. f) Schematic illustration of the intercalation chemistry for  $\alpha$ -MoO<sub>3</sub> and the WP-MoO<sub>3</sub>. Reproduced with permission from Ref. [72]. Copyright (2020) Wiley-VCH. g) Electrochemical performance of the alkali-acid Zn-MoO<sub>3</sub> hybrid battery. Reproduced with permission from Ref. [75]. Copyright (2021) American Chemical Society.

surface engineering strategy of MoO<sub>3</sub> is usually adopted. In the strategy of replacing electrolytes, He et al.<sup>[37b]</sup> improved the stability of the MoO<sub>3</sub> cathode by using quasi-solid polyvinyl alcohol (PVA)/ZnCl<sub>2</sub> gel electrolyte. The stability of the MoO<sub>3</sub> cathode in the quasi-solid electrolyte was significantly improved. The capacity retention rate of the MoO<sub>3</sub> cathode was significantly increased from 27.1% (in water-electrolyte) to 70.4% (in gel electrolyte) after 400 charge-discharge cycles (Figure 7a). The GCD curve of the MoO<sub>3</sub> cathode in the quasi-solid electrolyte is shown in Figure 7(b). The storage mechanism of Zn<sup>2+</sup> in the MoO<sub>3</sub> cathode in the gel electrolyte and the aqueous electrolyte is consistent. Although the Zn<sup>2+</sup> storage capacity decreases in gel electrolytes, it still greatly exceeds most ZIBs and other aqueous batteries (Figure 7c). On the modification of the electrolyte, Wang et al.<sup>[70]</sup> and Dunkin et al.<sup>[71]</sup> introduced a 30 M ZnCl<sub>2</sub> electrolyte into ZIBs with MoO<sub>3</sub> nanobelts cathode. In-situ XRD, XAS, and other experiments explained the enhanced charge storage mechanism of MoO<sub>3</sub> cathode in water-in-salt electrolytes. A high concentration of water-in-salt electrolyte inhibits the dissolution of MoO<sub>3</sub> nanobelts and the side reaction on the Zn anode. In the surface engineering strategy of MoO<sub>3</sub> cathode, Zhang et al.<sup>[72]</sup> prepared WP-MoO<sub>3</sub> by co-intercalating hydrated hydrogen ions into  $\alpha$ -MoO<sub>3</sub> nanoparticles by taking electrochemical linear sweep

voltammetry (Figure 7f). WP-MoO<sub>3</sub> with H<sub>3</sub>O<sup>+</sup> as the charge carrier is stored through the Grothuss mechanism (proton hopping transport between water molecules) in a Zn//WP-MoO<sub>3</sub> battery. The capacity retention rate increases from 42.2% of Zn//MoO<sub>3</sub> to 77.5% of Zn//WP-MoO<sub>3</sub> when the current density increases from 0.4 to 4.8 Ag<sup>-1</sup>. After 1000 cycles, the capacity retention rate of Zn//WP-MoO<sub>3</sub> increases from 13% to 83%, and the cycle stability is significantly improved. The surface engineering strategy of the MoO<sub>3</sub> cathode and replacing electrolyte strategy are combined to overcome the problems of the MoO<sub>3</sub> cathode in ZIBs. Liu et al.<sup>[73]</sup> prepared P-MoO<sub>3-x</sub>@Al<sub>2</sub>O<sub>3</sub> cathode in ZIBs. The synergistic effect of an Al<sub>2</sub>O<sub>3</sub> coating and a phosphating process prepares the P-MoO<sub>3-x</sub>@Al<sub>2</sub>O<sub>3</sub> cathode. Compared to Zn//MoO<sub>3</sub> (115.8 mAh g<sup>-1</sup>; 19.7%), Zn//P-MoO<sub>3-x</sub>@Al<sub>2</sub>O<sub>3</sub> has a specific capacity of 257.7 mAh g<sup>-1</sup> at a current density of 1 Ag<sup>-1</sup>. The capacity retention rate of Zn//P-MoO<sub>3-x</sub>@Al<sub>2</sub>O<sub>3</sub> is 57% when the current density increases to 20 Ag<sup>-1</sup>. Moreover, the quasi-solid-state fibrous ZIBs prepared with polyvinyl alcohol gel electrolyte have a capacity of 19.2 mAh cm<sup>-3</sup> and a high energy density of 240 Wh kg<sup>-1</sup> and 14.4 mWh cm<sup>-3</sup> (Figure 7d). Shi et al.<sup>[74]</sup> prepared oxygen-deficient MoO<sub>3-x</sub>/MXene composite membranes by adding MXene to MoO<sub>3</sub> nanofibers, and using a 2 M zinc trifluoromethanesulfonate (Zn(OTf)<sub>2</sub>) electrolyte to reduce the

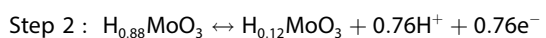
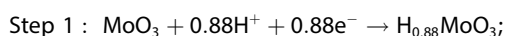
solubility of  $\text{MoO}_3$ . The  $\text{MoO}_{3-x}/\text{MXene}$  cathode delivers an ultra-high capacity of  $369.8 \text{ mAh g}^{-1}$  at a current density of  $0.2 \text{ A g}^{-1}$ , and the capacity retention rate is 46.7% after 1600 cycles. The  $\text{MoO}_{3-x}/\text{MXene}$  composite film cathode, Zn@MXene anode, and  $\text{Zn}(\text{OTf})_2$ -PVA gel electrolyte were assembled into micro-ZIBs by laser engraving technology. The micro-ZIBs with extremely self-healing, high flexibility, and a capacity retention rate of 62.7% after 2000 cycles at  $1.60 \text{ A cm}^{-2}$  were successfully prepared. Cai et al.<sup>[75]</sup> reported preparing an alkali-acid Zn- $\text{MoO}_3$  hybrid battery (Figure 7g). The  $\text{MoO}_3$  cathode uses a defective porous  $\text{MoO}_3$  nanobelt to reduce the storage barrier of  $\text{H}^+$  intercalation-deintercalation and improve the conductivity. The GCD curve of porous  $\text{MoO}_3$  nanobelts is shown in Figure 7(g). At the same time, the zinc anode achieves alkaline conversion of  $\text{OH}^-$  in an alkali-acid Zn- $\text{MoO}_3$  hybrid battery. The alkali-acid Zn- $\text{MoO}_3$  hybrid battery enables the coexistence of  $\text{H}^+$  and  $\text{OH}^-$  in the same system with an open circuit voltage of up to 1.85 V. High electrochemical performance with  $158 \text{ mAh g}^{-1}$  capacity at a current density of  $5 \text{ A g}^{-1}$  and 90% capacity retention after 200 cycles in alkali-acid Zn- $\text{MoO}_3$  hybrid battery.

### 3.5. Aqueous hydrogen-ion batteries

In aqueous hydrogen ion batteries (proton batteries), compared with traditional metal cations as charge carriers, protons as charge carriers have the smallest ionic radius (0.89 fm) and atomic mass. It is easier to intercalate in electrode materials, and the cost of hydrogen content is almost lower than that of the most abundant elements (the proportion of hydrogen in the earth's crust is ten times that of lithium). Moreover, proton batteries use an aqueous solution as an electrolyte solvent. Aqueous electrolyte avoids the pollution of toxic organic electrolytes to the environment and assembles proton batteries in an aqueous oxygen-containing climate.<sup>[76]</sup>  $\text{MoO}_3$  cathode has a high-rate performance in proton batteries due to its layered structure and multivalent redox reaction. However, the energy storage mechanism of the  $\text{MoO}_3$  cathode has yet to be revealed, which hinders its wide application. In some reports, it is considered that the energy storage and conversion of  $\text{MoO}_3$  cathode in proton batteries are achieved by intercalation of bare  $\text{H}^+$ . In contrast, other pieces think the  $\text{MoO}_3$  cathode reaches energy storage by co-intercalating hydrated hydrogen ions ( $\text{H}_3\text{O}^+$ ). Similar to aqueous ZIBs, the  $\text{MoO}_3$  cathode in proton batteries has problems such as severe dissolution and capacity decay during cycling. Improvement strategies usually use concentrated, gel, and quasi-solid electrolytes or coat the electrode surface with polymers or ceramics. The following will explore the fast proton transport mechanism of  $\text{MoO}_3$  and the advantages of using high and low-voltage redox reactions to assemble symmetrical proton complete battery applications.

In recent studies, Ma et al.<sup>[77]</sup> revealed the fast proton transport mechanism of the  $\text{MoO}_3$  cathode through experiments and theoretical calculations. Similar to the Grothuss proton transport mechanism of water molecules, protons form a hydrogen bond network in the  $\alpha\text{-MoO}_3$  cathode lattice of the

ultra-concentrated double-ion electrolyte ( $32 \text{ mol kg}^{-1} \text{ ZnCl}_2$  and  $1 \text{ mol kg}^{-1} \text{ P}_2\text{O}_5/\text{H}_2\text{O}$ ). The  $\alpha\text{-MoO}_3$  cathode achieves a fast proton transport Grothuss mechanism in the host material without lattice water. Theoretical calculations attribute the GCD curve asymmetry to the asymmetric protonation process (Figure 8a). In-situ XRD characterization results show that the interlayer spacing of  $\alpha\text{-MoO}_3$  remains almost unchanged during charge and discharge (Figure 8b). The nearly constant layer spacing in  $\alpha\text{-MoO}_3$  differs from the 11% expanded interlayer spacing co-intercalated in  $\alpha\text{-MoO}_3$  with  $\text{H}_3\text{O}^+$ . This result further proves that the  $\alpha\text{-MoO}_3$  cathode stores energy through the Grothuss mechanism of asymmetric bare  $\text{H}^+$  in proton batteries. In terms of electrolyte selection, the ultra-concentrated dual-ion electrolyte exhibits a more stable CV curve and negligible polarization (Figure 8c). The ultra-concentrated dual-ion electrolyte inhibits the dissolution and improves the cycle stability of  $\alpha\text{-MoO}_3$ , which is far superior to other aqueous ZIBs and proton batteries. In other reports, it is believed that the  $\text{MoO}_3$  cathode achieves energy storage through the participation of  $\text{H}_3\text{O}^+$ . Guo et al.<sup>[78]</sup> investigated  $\text{MoO}_3$  achieves energy storage in 4.4 M  $\text{H}_2\text{SO}_4$  electrolytes through the adsorption-desorption of  $\text{H}_3\text{O}^+$  on the surface and the intercalation of protons inside  $\text{MoO}_3$  internal. The EQCM in-situ mass monitoring results show that the transport direction of bare protons inside  $\text{MoO}_3$  inner is opposite to that of  $\text{H}_3\text{O}^+$  on the surface (Figure 8h).  $\text{MoO}_3$  adsorbs water during the process of proton intercalation, and the mass of  $\text{MoO}_3$  increases. In this report, the two-phase reaction of the  $\text{MoO}_3$  electrode during the cycle is also described in detail. The report of symmetrical proton full battery with  $\text{MoO}_3$  as working electrode and counter electrode. Wang et al.<sup>[9b]</sup> investigated the intercalation reaction of ultra-high rate  $\text{MoO}_3$  electrodes in a three-electrode system. The three-electrode system consists of 1 M  $\text{H}_2\text{SO}_4$  as an electrolyte,  $\text{MoO}_3$  as the working electrode, and  $\text{MoO}_3$  as the counter electrode. The energy storage mechanism of  $\text{MoO}_3$  is shown in Figure 8(d), and the ex-situ XRD test results are shown in Figure 8(f). The first discharge is to  $-0.5 \text{ V}$  (1 mode), and the proton cannot be extracted entirely to  $0.3 \text{ V}$  during the charging process (4 mode). The interlayer spacing of  $\text{MoO}_3$  increases with the decrease of the interlayer spacing, which is due to the strong electrostatic interaction between the proton and the  $\text{MoO}_6$  octahedron. Combined with XPS test results and the GCD curve in Figure 8(e), the energy storage mechanism is summarized as follows:



Xu et al.<sup>[79]</sup> prepared metallic  $\text{H}_{1.75}\text{MoO}_3$  nanobelts by electrochemically activating protons interaction in  $\text{MoO}_3$  to cause strong Jahn-Teller electron-phonon coupling. The high-resolution HAADF STEM images of  $\text{H}_{1.75}\text{MoO}_3$  and  $\text{H}_{1.75}\text{MoO}_3$  at charged 0.5 V showed that both maintain an orthorhombic symmetry structure. The formation of a hydrogen bond network in  $\text{MoO}_3$  nanobelts can transport protons spontaneously. The symmetrical proton full battery is assembled using  $\text{MoO}_3$

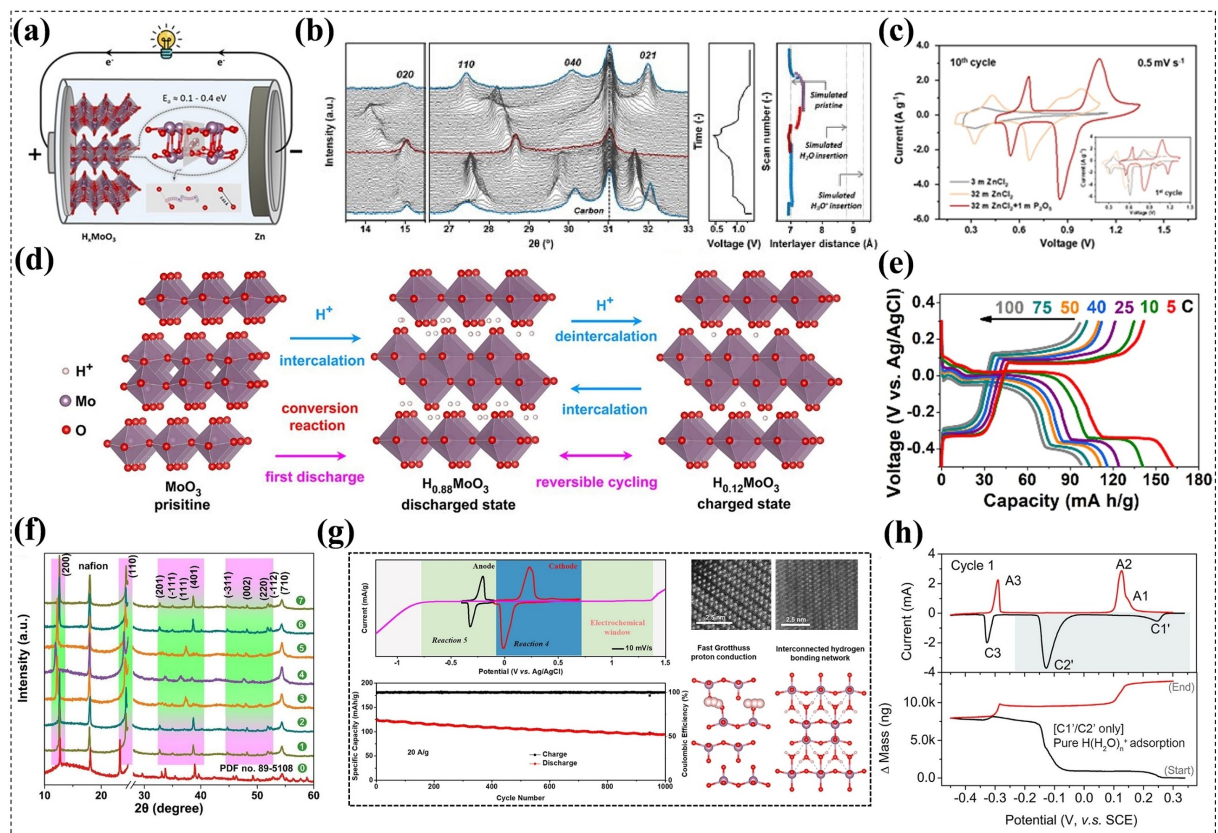


**Figure 8.** a) Application of  $\alpha$ -MoO<sub>3</sub> cathode in proton battery. b) In situ XRD patterns and interlayer-distance change upon protonation and deprotonation of MoO<sub>3</sub>. c) The CV curves of  $\alpha$ -MoO<sub>3</sub> using different electrolytes. Reproduced with permission from Ref. [77]. Copyright (2022) Wiley-VCH. d) Schematic illustrations of H<sup>+</sup> ions intercalation-deintercalation into MoO<sub>3</sub>. e) GCD curves of  $\alpha$ -MoO<sub>3</sub> at different rates. f) Ex-situ XRD patterns of the MoO<sub>3</sub> during the charge-discharge cycle. Reproduced with permission from Ref. [9b]. Copyright (2018) Wiley-VCH. g) The MoO<sub>3</sub>-based symmetrical proton ion entire cell. h) EQCM results for MoO<sub>3</sub> anodes. Reproduced with permission from Ref. [78]. Copyright (2020) Elsevier.

low-voltage redox reaction as the anode and high-voltage redox reaction as the cathode, as shown in Figure 8(g). After 1000 cycles, the full battery has a cycle stability of 75 % of the initial capacity. It provides a high energy density of 14.7 Wh kg<sup>-1</sup> at an ultra-high-power density of 12.7 kW kg<sup>-1</sup>, which is superior to many fast-charging supercapacitors and lead-acid batteries. The application of molybdenum trioxide-based cathode in aqueous hydrogen ion batteries is shown in Table 3.

### 3.6. Aqueous aluminum-ion batteries

In aluminum ion batteries (AlBs), the reversible intercalation-deintercalation of aluminium ions (Al<sup>3+</sup>) by MoO<sub>3</sub> electrode was first reported by Lahan et al.<sup>[80]</sup> in 2019. The AlBs have attracted significant attention due to the richest content of aluminum metal resources and the high theoretical capacity (8040 mAh cm<sup>-3</sup>) of Al<sup>3+</sup> as a charge carrier involving three-electron transfer. Because the reduction potential of Al (-1.66 V vs. SHE) is lower than the water electrolysis potential, the electrolyte is mainly concentrated on the ionic liquid electrolyte. Ionic liquids are highly corrosive, so people have developed aqueous AlB.<sup>[81]</sup> In aqueous electrolytes, few elec-

trode materials can reversibly insert and extract Al<sup>3+</sup>. As a typical intercalation material, MoO<sub>3</sub> has been developed as a cathode material for aqueous AlBs. Lahan et al.<sup>[80]</sup> demonstrate that Al<sup>3+</sup> is reversibly intercalated into MoO<sub>3</sub> using a three-electrode system. Comparing different electrolytes of 1 M AlCl<sub>3</sub>, 1 M AlNO<sub>3</sub>, and 0.5 M Al<sub>2</sub>(SO<sub>4</sub>)<sub>3</sub> in dissolved water, the MoO<sub>3</sub> cathode has better stability in the 1 M AlCl<sub>3</sub> electrolytes. To improve the reversible storage capacity of MoO<sub>3</sub> for Al<sup>3+</sup> in aqueous electrolytes, another study in this group.<sup>[82]</sup> by combining MoO<sub>3</sub> with graphene and adding diethylene glycol dimethyl ether (50:50 v/v) to the electrolyte, the performance is about 60 % higher than the initial capacity after 100 cycles. The standard crystal structures of MoO<sub>3</sub> include  $\alpha$ -MoO<sub>3</sub>,  $\beta$ -MoO<sub>3</sub>, and  $h$ -MoO<sub>3</sub> can be used as electrode materials for aqueous AlBs. Hsu et al.<sup>[17]</sup> characterized the different crystal structures of MoO<sub>3</sub> during Al<sup>3+</sup> intercalation by in-situ XAS and XRD techniques. Among them,  $\alpha$ -MoO<sub>3</sub> has a higher Al<sup>3+</sup> storage capacity, as shown in the CV curve in Figure 9(b). The  $h$ -MoO<sub>3</sub> cycle process with tunnel structure has better stability. The octahedral MoO<sub>6</sub> of  $h$ -MoO<sub>3</sub> is arranged around the NH<sub>4</sub><sup>+</sup> molecule. The structure of  $h$ -MoO<sub>3</sub> is seen from the z-axis direction, as shown in Figure 9(a). The in-situ Mo K-edge XANES spectrum of  $h$ -MoO<sub>3</sub> during the voltammetric cycle is shown in Figure 9(c). The peak labeled a corresponds to the transition of

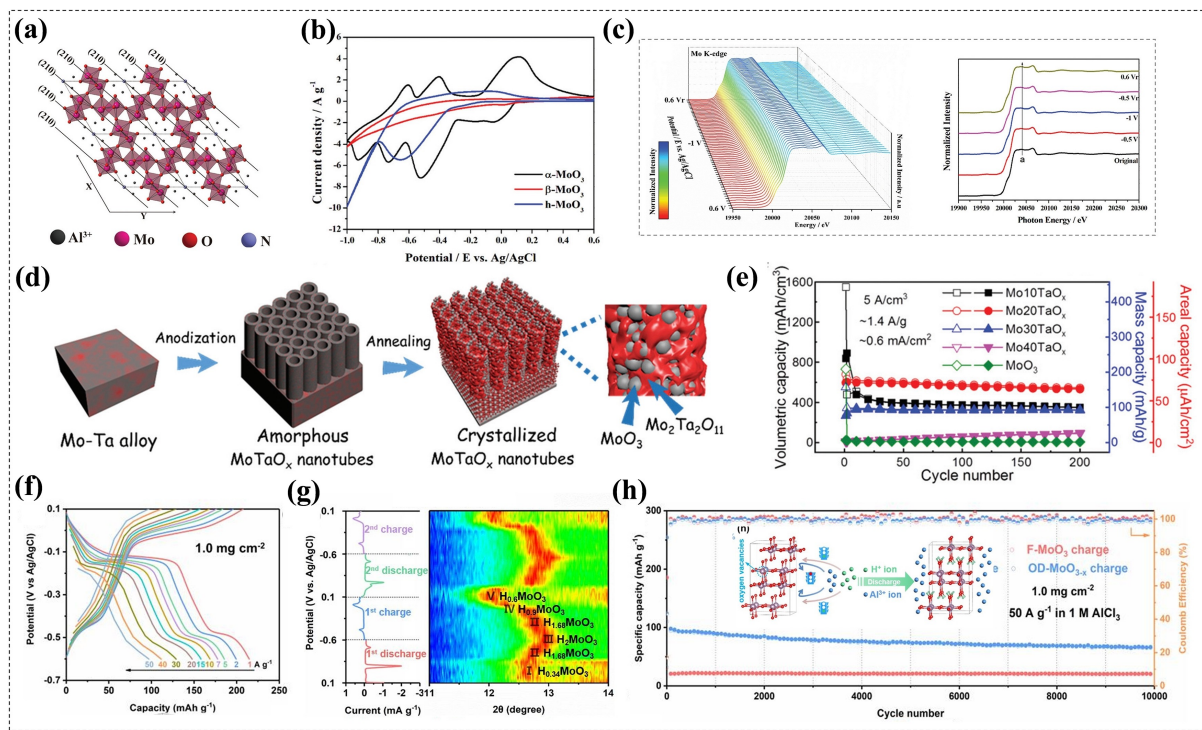


**Figure 9.** a)  $h\text{-MoO}_3$ , b) CV curves of various crystal phases of  $\text{MoO}_3$ , c) Mo K-edge XANES curves of  $h\text{-MoO}_3$  at various potentials. Reproduced with permission from Ref. [17]. Copyright (2022) Royal Society of Chemistry. d) Schematic illustration of the synthesis process of  $\text{MoTaO}_x$ . e) Cycling performance of  $\text{MoTaO}_x$  and  $\text{MoO}_3$ . Reproduced with permission from Ref. [83]. Copyright (2021) Royal Society of Chemistry. f) GCD curves of OD- $\text{MoO}_{3-x}$  at various current densities, and g) the corresponding contour plots for in situ XRD patterns of OD- $\text{MoO}_{3-x}$  in 1 M  $\text{AlCl}_3$ . h) Long-term cyclic performance at  $50 \text{ A g}^{-1}$ . Reproduced with permission from Ref. [37c]. Copyright (2022) Elsevier.

the molybdenum 1 s to the 5P orbit. The ion valence state is inferred from the absorption edge and energy spectrum position of the K-edge XANES spectrum. The  $h\text{-MoO}_3$  remains in its original form throughout the cycle, and the white line of the Mo K-edge XANES spectrum remains almost at 20040.8 eV (AVS value is about 5.57). The structure of  $\alpha\text{-MoO}_3$  and  $\beta\text{-MoO}_3$  was destroyed during the deintercalation process of  $\text{Al}^{3+}$ . Jin et al.<sup>[83]</sup> to improve the stability of the  $\text{MoO}_3$  cathode in aqueous AlIBs, one-dimensional  $\text{MoTaO}_x$  nanotubes (Figure 9d) were synthesized.  $\text{MoTaO}_x$  nanotubes synthesis through electrochemical oxidation of Mo-Ta alloy substrate, and  $\text{MoTaO}_x$  nanotubes showed better specific capacity and stability than the original  $\text{MoO}_3$  in aqueous electrolyte (Figure 9e).

The electrolyte of aqueous AlIBs contains  $\text{Al}^{3+}$  and  $\text{H}^+$ , and  $\text{H}^+$  with a smaller radius competes with  $\text{Al}^{3+}$  during the charge and discharge process. To improve the performance of  $\text{MoO}_3$  in aqueous AlIB, it is essential to explore the energy storage and conversion mechanism further. In a recent report, Huang et al.<sup>[37c]</sup> evaluated the energy storage mechanism of  $\text{MoO}_3$  (OD- $\text{MoO}_{3-x}$ ) in aqueous AlIBs by in-situ XRD, Raman, and pH monitoring during the cycle process of oxygen-containing defects  $\text{MoO}_3$  (OD- $\text{MoO}_{3-x}$ ) in AlIBs. This report shows that the  $\text{MoO}_3$  cathode in the aqueous AlIBs is stored by  $\text{H}^+$  insertion and  $\text{Al}^{3+}$  adsorption (Figure 9h illustration). Similar to  $\text{Li}^+$  intercalation, it was characterized by in-situ XRD (Figure 9g). The irreversible capacity fading during the cycle is mainly attributed to the incomplete deintercalation of  $\text{H}^+$ . The 1 M

$\text{AlCl}_3$  aqueous solution with higher conductivity than  $\text{Al}_2(\text{SO}_4)_3$  and  $\text{Al}(\text{NO}_3)_3$  at the same concentration was selected as the electrolyte. The galvanostatic charge-discharge curve of OD- $\text{MoO}_{3-x}$  was shown in Figure 9(f) in the voltage window of 0.1 to  $-0.6 \text{ V}$ . The prepared oxygen-containing defect OD- $\text{MoO}_{3-x}$  has excellent rate performance ( $97 \text{ mAh g}^{-1}$  at a current density of  $50 \text{ A g}^{-1}$  for only 7 s) and a capacity retention rate of 69% after 10000 cycles at  $50 \text{ A g}^{-1}$  (Figure 9h). The application of molybdenum trioxide-based cathode in aqueous aluminum ion batteries is shown in Table 3.

In summary, compared with other cathode materials,  $\text{MoO}_3$  cathode has great advantages in aqueous and non-aqueous rechargeable ion batteries due to its unique crystal structure and high theoretical capacity. In non-aqueous lithium-ion batteries, the  $\text{MoO}_3$  cathode based on the pseudocapacitance characteristics can perform rapid charge and discharge during the lithium-ion intercalation reaction. In non-aqueous magnesium and calcium ion batteries, the  $\text{MoO}_3$  cathode can not only be compatible with complex electrolytes, but also the large interlayer spacing allows reversible intercalation and deintercalation of large-sized  $\text{Mg}^{2+}$  and  $\text{Ca}^{2+}$  ions.  $\text{MoO}_3$  also shows its high-rate storage advantages in emerging aqueous zinc, hydrogen and aluminum ion batteries.

## 4. Performance Optimization Strategy

A series of optimization strategies were adopted to improve the inherent poor conductivity and limited cycle stability of  $\text{MoO}_3$  as a transition metal oxide (Figure 10). In the past reports on the application of  $\text{MoO}_3$  cathode in rechargeable ion batteries, methods such as the preparation of nanostructures, defect engineering, pre-intercalation of ions, and conductive materials composite were used to optimize the electrochemical performance of  $\text{MoO}_3$  cathode (Figure 10). Among them, the preparation of nanostructures can increase the stress and the increase contact area between  $\text{MoO}_3$  and electrolyte, which can significantly shorten the ion diffusion path. The introduction of oxygen vacancies in  $\text{MoO}_3$  can improve the conductivity of  $\text{MoO}_3$  and promote charge transfer during the ion storage process. Pre-intercalated ions can effectively support the layered structure of  $\text{MoO}_3$  to improve structural stability. But, the inherent poor conductivity of  $\text{MoO}_3$  cannot be solved only by structural design, so it is often compounded with conductive materials for further optimization performance. Each optimization strategy is described in detail below.

### 4.1. Preparation of nanostructures

From past reports, we know that the electrochemical performance of the battery is closely related to the microstructure of the electrode. In storing  $\text{Li}^+$  and  $\text{H}^+$  ions, the intercalation ions in the  $\text{MoO}_3$  cathode cannot be completely deintercalated. Irreversible capacity loss and low initial coulombic efficiency in the first cycle need to be tuned by adjusting the nanostructure of the  $\text{MoO}_3$ -based electrode material. The preparation of nanostructured  $\text{MoO}_3$  through different experimental schemes has been used as a general strategy to improve  $\text{MoO}_3$  electrode materials. When  $\text{MoO}_3$  is grown from bulk to nanoscale, the

diffusion path of ions is significantly shortened, the active sites of ions are enriched, and the contact area between the electrode and the electrolyte is increased. Also, nanostructures can dramatically enhance the stress of  $\text{MoO}_3$  and are more adaptable to volume changes during cycling, thereby improving the electrochemical performance of  $\text{MoO}_3$ . According to the size of nanostructures, they are divided into 0D nanoparticles, 1D nanobelts, nanotubes, 2D nanosheets, etc. (Figure 11). In the study of Li et al.,<sup>[96]</sup> Density functional theory calculation systematically studied the adsorption and diffusion behavior of  $\text{Li}^+$  ions on  $\text{MoO}_3$  with different dimensions. Compared with bulk  $\text{MoO}_3$ , 1D nanobelts and 2D monolayer  $\text{MoO}_3$  as cathode materials for LIBs have high  $\text{Li}^+$  ion binding energy and low  $\text{Li}^+$  ion diffusion barrier. Therefore, low-dimensional nanosized  $\text{MoO}_3$  has better electronic conductivity, fast  $\text{Li}^+$  ion diffusion, higher operating voltage, and energy density.

In the study of  $\text{MoO}_3$  with 0D nanostructures (Figures 11a and 11b), Lee et al.<sup>[92]</sup> prepared  $\text{MoO}_3$  nanoparticles by hot-wire chemical vapor deposition (HWCVD). The TEM images of  $\text{MoO}_3$  nanoparticles with a diameter of 5–20 nm are shown in Figure 11(a). Compared with the rapid capacity decay of 5  $\mu\text{m}$  large size  $\text{MoO}_3$ ,  $\text{MoO}_3$  nanoparticles prepared by HWCVD provide a shorter lithium ion diffusion path, and no capacity decay occurs after 150 cycles. Zhao et al.<sup>[97]</sup> uniformly anchored  $\alpha\text{-MoO}_3$  nanoparticles with a size of 1–3 nm to carbon nanofibers by electrospinning. The prepared nanocomposites ( $\text{MoO}_3/\text{CCNFs}$ ) effectively overcome the problems of the  $\text{MoO}_3$  intercalation of lithium ions. In the study of 1D nanostructured  $\text{MoO}_3$  (Figures 11c and d), the pervasive 1D nanobelts are usually prepared by the hydrothermal method. In the second chapter, Yao et al.<sup>[19]</sup> prepared ultra-long  $\alpha\text{-MoO}_3$  nanobelts by hydrothermal reaction (Figure 11b). Liu<sup>[73]</sup> grew vertically aligned nanorods on carbon cloth by a simple hydrothermal reaction, as shown in Figure 11(d). Hu et al.<sup>[98]</sup> synthesized single-walled  $\text{MoO}_3$  nanotubes for the first time by thiol-

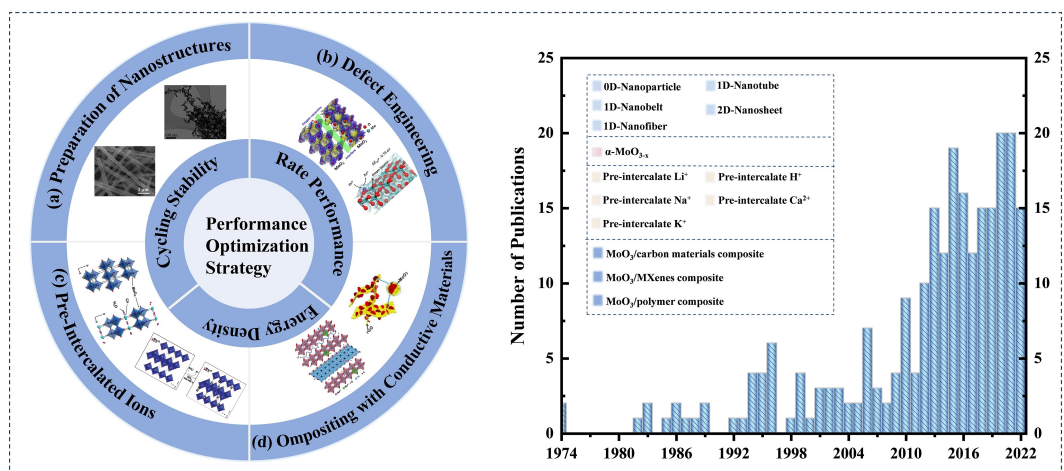


**Figure 10.** a) Preparation of nanostructures. Reproduced with permission from Ref. [19]. Copyright (2016) WILEY-VCH. Reproduced with permission from Ref. [92]. Copyright (2008) WILEY-VCH. b) Defect engineering. Reproduced with permission from Ref. [73]. Copyright (2020) WILEY-VCH. Reproduced with permission from Ref. [93]. Copyright (2018) American Chemical Society. c) Pre-intercalated ions. Reproduced with permission from Ref. [39]. Copyright (2013) WILEY-VCH. Reproduced with permission from Ref. [68]. Copyright (2020) American Chemical Society. d) Compositing with conductive materials. Reproduced with permission from Ref. [94]. Copyright (2021) WILEY-VCH. Reproduced with permission from Ref. [95]. Copyright (2018) Royal Society of Chemistry.

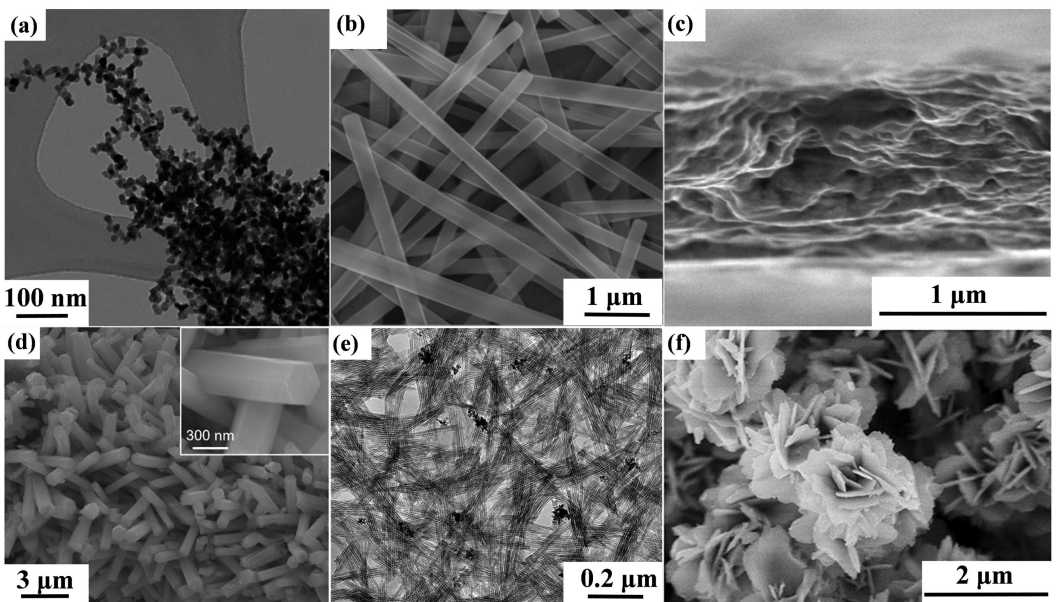


**Figure 11.** a)  $\text{MoO}_3$  nanoparticle. Reproduced with permission from Ref. [92]. Copyright (2008) WILEY-VCH. b)  $\text{MoO}_3$  nanobelt. Reproduced with permission from Ref. [19]. Copyright (2016) WILEY-VCH. c)  $\text{MoO}_3$  nanosheet. Reproduced with permission from Ref. [32]. Copyright (2016) Springer Nature. d)  $\text{MoO}_3$  nanorod. Reproduced with permission from Ref. [73]. Copyright (2020) WILEY-VCH. e) Single-Walled  $\text{MoO}_3$  Nanotube. Reproduced with permission from Ref. [98]. Copyright (2008) American Chemical Society. f)  $\text{MoO}_3$  nanoflower. Reproduced with permission from Ref. [99]. Copyright (2021) Springer Nature.

assisted hydrothermal reaction. TEM images are shown in Figure 11(e). In the study of 2D nanostructured  $\text{MoO}_3$  (Figure 11e and f). In addition to the  $\text{MoO}_3$  nanosheets prepared by the liquid-phase exfoliation method in the second chapter.<sup>[32]</sup> Wei et al.<sup>[99]</sup> prepared  $\text{MoO}_3$  nanosheets by the one-step solvothermal method. The obtained nanosheets form nanoflowers, as shown in Figure 11(f). Both theoretical and experimental results show that this unique two-dimensional nanosheet flower structure reduces the lithium-ion diffusion path and facilitates  $\text{Li}^+$  intercalation. When used as an electrode material for LIBs, it exhibits higher reversible lithium storage capacity and long-cycle stability.

#### 4.2. Defect engineering

Defect engineering mainly focuses on introducing oxygen defects in  $\text{MoO}_3$ , which can significantly improve the conductivity of  $\text{MoO}_3$ . The Mo3d orbit of  $\text{MoO}_3$  is discontinuous at the Fermi level, and its noticeable band gap shows its semiconductor properties. Therefore, as an electrode material,  $\text{MoO}_3$  has poor conductivity and slow electrochemical reaction kinetics. Theoretically, Hao et al.<sup>[93]</sup> calculated the density of states (DOS) by density functional theory (DFT). The DOS comparison diagram shows that  $\text{MoO}_2$  has metallic properties, while  $\alpha\text{-MoO}_3$  has semiconductor properties. The introduction of oxygen vacancies will cause new occupied states in the band gap of  $\alpha\text{-MoO}_3$  so that  $\alpha\text{-MoO}_3$  changes from semiconductor to metal properties, as shown in Figure 10(b). The reason for the increase in conductivity is that when there are oxygen defects,  $\text{Mo}^{6+}$  must be reduced to  $\text{Mo}^{5+}$  to maintain electrical neutrality. The empty 4d band before  $\alpha\text{-MoO}_3$  is occupied by

electrons. The work function of  $\alpha\text{-MoO}_3$  decreases with the increase of oxygen vacancies, and the conductivity is improved. In the study of Zhang et al.,<sup>[94]</sup>  $\alpha\text{-MoO}_{3-x}$  with oxygen vacancies has much lower Li-ion adsorption energy than the original  $\alpha\text{-MoO}_3$ . The  $\text{Li}^+$  diffusion barrier of  $\text{MoO}_3$  with oxygen vacancies is much smaller than that of  $\alpha\text{-MoO}_3$  without oxygen vacancies. The introduction of oxygen vacancies in  $\alpha\text{-MoO}_3$  facilitates charge transfer and  $\text{Li}^+$  diffusion during lithium storage.

The introduced oxygen defects can enhance the intercalation pseudocapacitance of  $\text{MoO}_3$  as cathode material in LIBs. Kim et al.<sup>[18]</sup> compared oxygen-defective orthorhombic molybdenum trioxide  $\text{R-MoO}_{3-x}$  with fully oxidized  $\alpha\text{-MoO}_3$ . The oxygen-defective  $\text{R-MoO}_{3-x}$  can significantly improve the charge storage of the intercalation pseudocapacitance based on the Faraday reaction. The formula calculation  $b=1$  is not limited by diffusion, and the capacity loss during the cycle is small. The stability is significantly improved. Zhang et al.<sup>[46]</sup> characterized by in-situ XRD experiments that the structure of  $\text{MoO}_3$  with oxygen vacancies is not easily destroyed during the  $\text{Li}^+$  intercalation process, and the cycle stability is significantly enhanced. In the cathode application of aqueous ZIBs,  $\text{MoO}_3$  with oxygen vacancies is more conducive to the adsorption and desorption of  $\text{Zn}^{2+}$ . As shown in Figure 10(b),  $\text{MoO}_3$  containing oxygen vacancies is more conducive to the reversible storage of  $\text{Zn}^{2+}$ .<sup>[73]</sup> The method of introducing oxygen vacancies in  $\alpha\text{-MoO}_3$ , in addition to the improvement of the typical preparation method in the second chapter, has processes such as hydrazine hydrate reduction, plasma etching, annealing reduction and phosphating annealing. In the method of introducing oxygen defects by hydrazine hydrate reduction. Yingying Zhang et al. by slowly dropping hydrazine hydrate solution with extremely strong reducibility into the aqueous

dispersion of  $\alpha$ -MoO<sub>3</sub> nanobelts added with hydrochloric acid at room temperature under continuous stirring. The color of MoO<sub>3</sub> nanobelts changed from white to dark blue, indicating the introduction of oxygen vacancies. Subsequently, the surface of oxygen-containing vacancy  $\alpha$ -MoO<sub>3-x</sub> was modified with polydiallyldimethylammonium chloride (PDDA) to change the surface of the nanobelt from negative to positive, to further combine with negatively charged MXene through the electrostatic assembly. Guobin Zhang et al. prepared oxygen-deficient  $\alpha$ -MoO<sub>3-x</sub> with an improved electrochemical performance by H<sub>2</sub> plasma etching of  $\alpha$ -MoO<sub>3</sub>. Among them, different etching time was introduced into the oxygen-deficient samples, and the crystal structure of  $\alpha$ -MoO<sub>3-x</sub> etched for 20 min was more stable, and brought larger Li<sup>+</sup> diffusion coefficient, lower charge transfer resistance, and minimum polarization.

### 4.3. Pre-intercalated ions

The pre-intercalated ions in MoO<sub>3</sub> can be used as pillars to alleviate the deformation of the MoO<sub>3</sub> structure during charging and discharging and enhance stability. In the application of LIBs cathode, Hu et al.<sup>[100]</sup> expanded the interlayer spacing of  $\alpha$ -MoO<sub>3</sub> by pre-embedding K<sup>+</sup> into  $\alpha$ -MoO<sub>3</sub>. As a LIBs cathode material, it accelerated the transmission of Li<sup>+</sup>. It had a capacity retention rate of 83.9% after 500 cycles at 1.5 A g<sup>-1</sup>, much higher than  $\alpha$ -MoO<sub>3</sub> without K<sup>+</sup>. Dong et al.<sup>[44]</sup> demonstrated that the pre-embedding of Na<sup>+</sup> in the  $\alpha$ -MoO<sub>3</sub> cathode can effectively suppress the irreversible phase transition of  $\alpha$ -MoO<sub>3</sub> and obtain a more stable  $\alpha$ -MoO<sub>3</sub> layered crystal structure in LIBs by in-situ XRD tests. In the study of Mai et al.,<sup>[37f]</sup> pre-embedded Li<sup>+</sup> was effectively proved to increase the conductivity of MoO<sub>3</sub>. Wang et al.<sup>[39]</sup> prepared ammoniated MoO<sub>3</sub> by a mild ammoniation method, as shown in Figure 10(c). The ammoniated MoO<sub>3</sub> exhibits better electrochemical performance than the initial MoO<sub>3</sub>, with a capacity of 250 mA h g<sup>-1</sup> and almost no decay after 300 cycles. In the application of non-aqueous CIBs, as described in Section 3, Ca<sup>2+</sup> doped  $\alpha$ -MoO<sub>3</sub> was prepared by the cation exchange method to enhance the ion diffusion kinetic rate and structural stability Figure 10(c).<sup>[68]</sup> Applying aqueous hydrogen ion batteries, after  $\alpha$ -MoO<sub>3</sub> is embedded with hydrogen ions by electrochemical activation,  $\alpha$ -MoO<sub>3</sub> nanobelts change from semiconductor properties to metal properties with higher conductivity.<sup>[79]</sup> Wustrow et al.<sup>[101]</sup> prepared fluorine-doped MoO<sub>2.8</sub>F<sub>0.2</sub> by fluorination of  $\alpha$ -MoO<sub>3</sub>. Compared with  $\alpha$ -MoO<sub>3</sub>, it has faster electrochemical reaction kinetics, significantly improved initial coulombic efficiency (94% after doping, 86% without doping) and cycle stability (10 cycles after doping, the capacity retention rate is 80%, 53% without doping).

### 4.4. Conductive material composite

It is challenging to solve the problem of poor conductivity of molybdenum trioxide as an electrode material only through structural design. Composite with carbon materials, polymers,

Mxene, and other conductive materials are one of the most commonly used modification strategies to optimize the conductivity<sup>[102]</sup> and cycle stability of the MoO<sub>3</sub> cathode. Composite carbon materials<sup>[103]</sup> include carbon nanotubes,<sup>[56,104]</sup> graphene,<sup>[54,95]</sup> which are used as substrates,<sup>[95]</sup> coatings,<sup>[100]</sup> or three-dimensional conductive networks<sup>[54]</sup> to combine with MoO<sub>3</sub>, thus playing a crucial role in the ion transport and structural stability of MoO<sub>3</sub>. In the composite with graphene, the MoO<sub>3</sub>/graphene self-supporting film prepared through rapid microwave hydrothermal reaction has higher cycle stability than the original.<sup>[54]</sup> Wang et al.<sup>[95]</sup> by vertically growing MoO<sub>3</sub> nanosheets on graphene, as shown in Figure 10(d), prepared the MoO<sub>3</sub>-graphene composite exhibited a capacity of about 1500 mA h g<sup>-1</sup> and a cycle life of up to 1000 times in lithium storage. Among the composites with carbon nanotubes, the CNT/ $\alpha$ -MoO<sub>3</sub> nanobelt composites with synergistic effect prepared by Wanzheng Lu et al.<sup>[104]</sup> showed significantly improved electrochemical performance than pure  $\alpha$ -MoO<sub>3</sub> as a cathode for LIBs.

Two-dimensional transition metal-carbon/nitride Mxene is a novel graphene-like material<sup>[105]</sup> with ultra-high electrical conductivity ( $\approx$  5000 S cm<sup>-1</sup>), large specific surface area, and large surface functional groups. In the study of Zhang et al.,<sup>[94]</sup> introducing MXenes nanosheets into MoO<sub>3</sub> nanoribbons accelerates the diffusion and conduction kinetics of ions and electrons in lithium-ion batteries, as shown in Figure 10(d). The two-dimensional heterojunction of amorphous MoO<sub>3</sub> grown on the surface of MXenes prepared by Yan et al.<sup>[106]</sup> breaks through the limitation of van der Waals interaction. It achieves large-capacity storage of 426 C g<sup>-1</sup> within 400 s in LIBs, similar to capacitors. Not only that, but MXenes also have a certain degree of hydrophobicity. In the study of Shi et al.,<sup>[74]</sup> MXenes were combined with MoO<sub>3</sub> as a cathode material for aqueous ZIBs. MXenes partially reduced MoO<sub>3</sub> to form oxygen vacancies and significantly reduced the dissolution of MoO<sub>3</sub>. The composite cathode has an ultra-high capacity of 369.8 mA h g<sup>-1</sup> at 0.20 A g<sup>-1</sup> and excellent cycle life.

Composite with polymers is one of the effective strategies to enhance MoO<sub>3</sub>-based cathodes with structural stability and conductivity. The selection of polymers includes polyaniline (PANI),<sup>[107]</sup> poly (ethylene oxide) (PEO),<sup>[108]</sup> polypyrrole (PPy),<sup>[109]</sup> polyethylene glycol (PEG).<sup>[48]</sup> The polymer is a conductive and buffering agent to alleviate the structural fragmentation of MoO<sub>3</sub> during the cycle effectively. Liu et al.<sup>[107]</sup> prepare polyaniline coated with MoO<sub>3</sub> by a simple one-step hydrothermal process. A thin layer of polyaniline (PANI) coated MoO<sub>3</sub> introduces oxygen vacancies and inhibits the dissolution of MoO<sub>3</sub>. PANI-MoO<sub>3</sub> nanoribbons have ultra-high cycle stability and a capacity retention rate of 95.5% after 6000 cycles for aqueous HIBs. In the study of Nadimicherla et al.,<sup>[108]</sup> MoO<sub>3</sub>/PEO composite nanobelts were used as cathode materials for LIBs. PEO, a polymer that acts as both a buffer and a conductive agent, significantly improves the electrochemical performance of MoO<sub>3</sub>.

## 5. Summary and Perspectives

This review summarizes the latest research progress of molybdenum trioxide cathode in non-aqueous lithium-ion, magnesium-ion, calcium-ion, aqueous zinc-ion, hydrogen-ion, and aluminum-ion batteries. Among them, the molybdenum trioxide cathode is more widely used in lithium-ion batteries based on the characteristics of pseudocapacitance. It shows high lithium storage capacity and rapid charge and discharge advantages. In contrast, the application in multivalent and hydrogen ion batteries is still in its infancy. Through in-situ characterization and experimental research during charging and discharging, molybdenum trioxide's storage mechanism and electrochemical reaction pathway have been better understood. This review summarized the excellent application potential of molybdenum trioxide cathode in lithium-ion batteries and post-lithium systems. Here, we briefly overview the application prospect of molybdenum trioxide-based cathode in rechargeable batteries.

- (1) Lithium-ion batteries are widely used in various fields, especially in electric vehicles, renewable energy, and other areas. Molybdenum trioxide-based cathode has the advantages of high lithium storage capacity and fast charge. Increased capacity due to Molybdenum trioxide intercalation pseudocapacitance characteristics is superior to the current commercial cathode. In non-aqueous magnesium and calcium ion batteries, molybdenum trioxide-based cathodes can be compatible with complex electrolytes. The molybdenum trioxide-based cathode is still in the initial exploration stage of emerging aqueous zinc ion, hydrogen ion, and aluminum ion battery systems. But, the molybdenum trioxide-based cathode shows its application potential in ultra-high-rate storage of hydrogen ions, zinc ions, and aluminum ions.
- (2) Although the molybdenum trioxide-based cathode has excellent potential in rechargeable ion batteries, it is still necessary to further clarify the energy storage mechanism in the emerging energy storage system. Through in-situ experiments and characterization, we further understand the reaction mechanism of molybdenum trioxide cathode and electrochemical reaction process, thus achieving continuous improvement of energy storage performance. Lithium, calcium, and hydrogen ions intercalated in the molybdenum trioxide cathode cannot be utterly deintercalated during the first cycle. In the initial cycle process, the incomplete deintercalation of charge calargewill leads to a largely irreversible capacity loss of molybdenum trioxide. The conductivity and cycle stability of the molybdenum trioxide-based cathode still need to be further improved to meet the practical application.
- (3) To realize the broader application of molybdenum trioxide-based cathodes in rechargeable ion batteries, in addition to regulating the electrolyte, a series of strategies have been adopted to optimize the electrochemical performance of molybdenum trioxide cathode. The preparation of nanostructures, defect engineering, pre-intercalation of ions, and compounding with conductive materials are effective

strategies for modifying molybdenum trioxide cathodes. Exploiting a simplified, low-cost, large-scale preparation method and an effective modification strategy are critical challenges for the future practical application of molybdenum trioxide-based cathodes.

Biographies:

## Acknowledgements

*This project was financially supported by: the Natural Science Foundation of Heilongjiang Province (Nos. HL2020A014 and ZD2009103), the National Natural Science Foundation of China (Nos. 22101163 and 52250710161), the Graduate Innovative Program of Harbin Normal University (No. HSDSSCX2022-53), and Key Laboratory of Engineering Dielectrics and Its Application (Harbin University of Science and Technology), Ministry of Education (KFM202005 and KF20171110).*

## Conflict of Interest

The authors declare that they have no conflict of interest.

## Data Availability Statement

The data that support the findings of this study are available from the corresponding author upon reasonable request.

**Keywords:** MoO<sub>3</sub> · cathode · rechargeable ion batteries · storage mechanism · synthesis

- [1] D. Larcher, J. M. Tarascon, *Nat. Chem.* **2015**, *7*, 19–29.
- [2] a) M.-C. Fan, Y. Zhao, Y.-Q. Kang, J. Wozny, Z. Liang, J.-X. Wang, G.-M. Zhou, B.-H. Li, N. Tavajohi, F.-Y. Kang, *Rare Met.* **2022**, *41*, 1595–1604; b) W. He, Q.-S. Xie, J. Lin, B.-H. Qu, L.-S. Wang, D.-L. Peng, *Rare Met.* **2022**, *41*, 1456–1476.
- [3] Y. Liang, H. Dong, D. Aurbach, Y. Yao, *Nat. Energy* **2020**, *5*, 646–656.
- [4] X. Liu, T. Ji, H. Guo, H. Wang, J. Li, H. Liu, Z. Shen, *Electrochim. Energy Rev.* **2021**, *5*, 401–433.
- [5] a) R. Huang, W. Wang, C. Zhang, P. He, Y. Han, N. Chen, J. Yan, *Chin. Chem. Lett.* **2022**, *33*, 3955–3960; b) Y. Liu, X. Wu, *Chin. Chem. Lett.* **2022**, *33*, 1236–1244.
- [6] a) C. Bai, F. Ning, S. Pan, H. Wang, Y. Li, M. Shen, X. Zhou, *Chin. Chem. Lett.* **2022**, *33*, 1095–1099; b) W. Yang, W. Yang, Y. Huang, C. Xu, L. Dong, X. Peng, *Chin. Chem. Lett.* **2022**, *33*, 4628–4634.
- [7] P. R. XianhongChen, X. Wu, S. Liang, J. Zhou, *Acta Phys. -Chim. Sin.* **2022**, *38*, 2111003–.
- [8] a) X. Chen, P. Ruan, X. Wu, S. Liang, J. Zhou, *Acta Physico Chimica Sinica* **2021**, *0*, 2111003–2111000; b) W. Nie, H. Cheng, Q. Sun, S. Liang, X. Lu, B. Lu, J. Zhou, *Small Methods* **2023**, e2201572.
- [9] a) Z. Su, W. Ren, H. Guo, X. Peng, X. Chen, C. Zhao, *Adv. Funct. Mater.* **2020**, *30*; b) X. Wang, Y. Xie, K. Tang, C. Wang, C. Yan, *Angew. Chem. Int. Ed.* **2018**, *57*, 11569–11573; *Angew. Chem.* **2018**, *130*, 11743–11747.
- [10] a) Z. Fang, X.-L. Zhang, X.-Y. Hou, W.-L. Huang, L.-B. Li, *Rare Met.* **2022**, *41*, 2268–2279; b) C.-C. Zhou, Z. Su, X.-L. Gao, R. Cao, S.-C. Yang, X.-H. Liu, *Rare Met.* **2021**, *41*, 14–20; c) T. Seaby, T.-E. Lin, Y.-X. Hu, Q.-H. Yuan, L.-Z. Wang, *Rare Met.* **2022**, *41*, 1771–1796.
- [11] a) J. Ding, S. A. Abbas, C. Hanmandlu, L. Lin, C.-S. Lai, P.-C. Wang, L.-J. Li, C.-W. Chu, C.-C. Chang, *J. Power Sources* **2017**, *348*, 270–280; b) G. Qu, J. Wang, G. Liu, B. Tian, C. Su, Z. Chen, J.-P. Rueff, Z. Wang, *Adv.*

- Funct. Mater.* **2019**, *29*; c) Z. Wang, S. Madhavi, X. W. Lou, *J. Phys. Chem. C* **2012**, *116*, 12508–12513; d) Q. Xia, H. Zhao, Z. Du, Z. Zeng, C. Gao, Z. Zhang, X. Du, A. Kulka, K. Świerczek, *Electrochim. Acta* **2015**, *180*, 947–956; e) W. Xia, Q. Zhang, F. Xu, L. Sun, *ACS Appl. Mater. Interfaces* **2016**, *8*, 9170–9177; f) C. Yang, X. Liu, Z. Yang, L. Gu, Y. Yu, *Adv. Mater. Interfaces* **2016**, *3*; g) H. Jiang, W. Shin, L. Ma, J. J. Hong, Z. Wei, Y. Liu, S. Zhang, X. Wu, Y. Xu, Q. Guo, M. A. Subramanian, W. F. Stickle, T. Wu, J. Lu, X. Ji, *Adv. Energy Mater.* **2020**, *10*.
- [12] a) Y. Li, H. Sun, X. Cheng, Y. Zhang, K. Zhao, *Nano Energy* **2016**, *27*, 95–102; b) K. Sakaushi, J. Thomas, S. Kaskel, J. Eckert, *Chem. Mater.* **2013**, *25*, 2557–2563.
- [13] a) H. Bräkken, *Zeitschrift für Kristallographie - Crystalline Materials* **1931**, *78*, 484–488; b) N. Wooster, *Zeitschrift für Kristallographie - Crystalline Materials* **1931**, *80*, 504–512.
- [14] a) N. Kumagai, N. Kumagai, K. Tanno, *Appl. Phys. A* **1989**, *49*, 83–89; b) I. J. Ramírez, A. Martínez-de la Cruz, *Mater. Lett.* **2003**, *57*, 1034–1039.
- [15] J. Song, X. Wang, X. Ni, H. Zheng, Z. Zhang, M. Ji, T. Shen, X. Wang, *Mater. Res. Bull.* **2005**, *40*, 1751–1756.
- [16] G. S. Zakharova, C. Schmidt, A. Ottmann, E. Mijowska, R. Klingeler, *J. Solid State Electrochem.* **2018**, *22*, 3651–3661.
- [17] F. H. Hsu, S. Y. Hsu, B. H. Chen, J. L. Chen, J. M. Chen, K. T. Lu, *Nanoscale* **2022**, *14*, 7502–7515.
- [18] H. S. Kim, J. B. Cook, H. Lin, J. S. Ko, S. H. Tolbert, V. Ozolins, B. Dunn, *Nat. Mater.* **2017**, *16*, 454–460.
- [19] B. Yao, L. Huang, J. Zhang, X. Gao, J. Wu, Y. Cheng, X. Xiao, B. Wang, Y. Li, J. Zhou, *Adv. Mater.* **2016**, *28*, 6353–6358.
- [20] Q.-L. Wu, S.-X. Zhao, L. Yu, X.-X. Zheng, Y.-F. Wang, L.-Q. Yu, C.-W. Nan, G. Cao, *J. Mater. Chem. A* **2019**, *7*, 13205–13214.
- [21] Z. Cui, W. Yuan, C. M. Li, *J. Mater. Chem. A* **2013**, *1*, 12926–12931.
- [22] J. Han, P. Liu, Y. Ito, X. Guo, A. Hirata, T. Fujita, M. Chen, *Nano Energy* **2018**, *45*, 273–279.
- [23] M. A. Spencer, O. Yıldız, I. Kamboj, P. D. Bradford, V. Augustyn, *Energy Fuels* **2021**, *35*, 16183–16193.
- [24] W. Zhang, H. Li, C. J. Kirby, M. Al-Hussein, A. Y. Elezzabi, *ACS Appl. Mater. Interfaces* **2019**, *11*, 20378–20385.
- [25] C. Wang, L. Wu, H. Wang, W. Zuo, Y. Li, J. Liu, *Adv. Funct. Mater.* **2015**, *25*, 3524–3533.
- [26] A. M. Hashem, S. M. Abbas, A. E. Abdel-Ghany, A. E. Eid, A. A. Abdel-Khalek, S. Indris, H. Ehrenberg, A. Mauger, C. M. Julien, *J. Alloys Compd.* **2016**, *686*, 744–752.
- [27] A. M. Hashem, A. E. Abdel-Ghany, R. S. El-Tawil, S. Indris, H. Ehrenberg, A. Mauger, C. M. Julien, *Nanomaterials (Basel)* **2019**, *10*.
- [28] J. H. Kim, D. S. Utomo, D. Lee, J. W. Choi, M. Song, *J. Power Sources* **2021**, *512*.
- [29] D. Hanlon, C. Backes, T. M. Higgins, M. Hughes, A. O'Neill, P. King, N. McEvoy, G. S. Duesberg, B. Mendoza Sanchez, H. Pettersson, V. Nicolosi, J. N. Coleman, *Chem. Mater.* **2014**, *26*, 1751–1763.
- [30] H. Zhang, L. Gao, Y. Gong, *Electrochim. Commun.* **2015**, *52*, 67–70.
- [31] A. S. Etman, L. Wang, K. Edström, L. Nyholm, J. Sun, *Adv. Funct. Mater.* **2019**, *29*.
- [32] X. Xiao, H. Song, S. Lin, Y. Zhou, X. Zhan, Z. Hu, Q. Zhang, J. Sun, B. Yang, T. Li, L. Jiao, J. Zhou, J. Tang, Y. Gogotsi, *Nat. Commun.* **2016**, *7*, 11296.
- [33] S. Sun, Q. Xia, J. Liu, J. Xu, F. Zan, J. Yue, S. V. Savilov, V. V. Lunin, H. Xia, *J. Materiomics* **2019**, *5*, 229–236.
- [34] X. Wen, W. Yang, Y. Ding, S. Niu, Z. L. Wang, *Nano Res.* **2013**, *7*, 180–189.
- [35] L. A. Riley, S.-H. Lee, L. Gedvilas, A. C. Dillon, *J. Power Sources* **2010**, *195*, 588–592.
- [36] a) I. A. de Castro, R. S. Datta, J. Z. Ou, A. Castellanos-Gomez, S. Sriram, T. Daeneke, K. Kalantar-Zadeh, *Adv. Mater.* **2017**, *29*; b) X. Hu, W. Zhang, X. Liu, Y. Mei, Y. Huang, *Chem. Soc. Rev.* **2015**, *44*, 2376–2404; c) C. V. Ramana, A. Mauger, C. M. Julien, *Prog. Cryst. Growth Charact. Mater.* **2021**, *67*; d) K. Tang, S. A. Farooqi, X. Wang, C. Yan, *ChemSusChem* **2019**, *12*, 755–771; e) J. Xie, H. Zhang, Q. Liu, X. Liu, X. Lu, *Mater. Today* **2020**, *8*.
- [37] a) T. Tsumura, M. Inagaki, *Solid State Ionics* **1997**, *104*, 183–189; b) X. He, H. Zhang, X. Zhao, P. Zhang, M. Chen, Z. Zheng, Z. Han, T. Zhu, Y. Tong, X. Lu, *Adv. Sci. (Weinh.)* **2019**, *6*, 1900151; c) W. Huang, K. Zhang, B. Yuan, L. Yang, M. Zhu, *Energy Storage Mater.* **2022**, *50*, 152–160; d) J. T. Incorvati, L. F. Wan, B. Key, D. Zhou, C. Liao, L. Fuoco, M. Holland, H. Wang, D. Prendergast, K. R. Poepelmeier, J. T. Vaughney, *Chem. Mater.* **2015**, *28*, 17–20; e) S. Kim, L. Yin, S. M. Bak, T. T. Fister, H. Park, P. Parajuli, J. Gim, Z. Yang, R. F. Klie, P. Zapol, Y. Du, S. H. Lapidus, J. T. Vaughney, *Nano Lett.* **2022**, *22*, 2228–2235; f) L. Mai, B. Hu, W. Chen, Y. Qi, C. Lao, R. Yang, Y. Dai, Z. L. Wang, *Adv. Mater.* **2007**, *19*, 3712–3716.
- [38] H. Pan, S. Zhang, J. Chen, M. Gao, Y. Liu, T. Zhu, Y. Jiang, *Mol. Syst. Des. Eng.* **2018**, *3*, 748–803.
- [39] X.-J. Wang, R. Nesper, C. Villevieille, P. Novák, *Adv. Energy Mater.* **2013**, *3*, 606–614.
- [40] M. Baldoni, L. Craco, G. Seifert, S. Leoni, *J. Mater. Chem. A* **2013**, *1*, 1778–1784.
- [41] T. Brezesinski, J. Wang, S. H. Tolbert, B. Dunn, *Nat. Mater.* **2010**, *9*, 146–151.
- [42] A. M. Hashem, M. H. Askar, M. Winter, J. H. Albering, J. O. Besenhard, *Ionics* **2007**, *13*, 3–8.
- [43] W. Li, F. Cheng, Z. Tao, J. Chen, *J. Phys. Chem. B* **2006**.
- [44] Y. Dong, X. Xu, S. Li, C. Han, K. Zhao, L. Zhang, C. Niu, Z. Huang, L. Mai, *Nano Energy* **2015**, *15*, 145–152.
- [45] C. V. Subba Reddy, E. H. Walker, C. Wen, S. i. Mho, *J. Power Sources* **2008**, *183*, 330–333.
- [46] G. Zhang, T. Xiong, M. Yan, L. He, X. Liao, C. He, C. Yin, H. Zhang, L. Mai, *Nano Energy* **2018**, *49*, 555–563.
- [47] X.-J. Wang, R. Nesper, C. Villevieille, P. Novák, *Adv. Energy Mater.* **2013**, *3*, 606–614.
- [48] C. V. Subba Reddy, E. H. Walker, C. Wen, S.-i. Mho, *J. Power Sources* **2008**, *183*, 330–333.
- [49] D. Yan, X. Luo, H. Zhang, G. Zhu, L. Chen, G. Chen, H. Xu, A. Yu, *J. Alloys Compd.* **2016**, *688*, 481–486.
- [50] M. A. Ibrahim, F. Y. Wu, D. A. Mengistie, C. S. Chang, L. J. Li, C. W. Chu, *Nanoscale* **2014**, *6*, 5484–5490.
- [51] X. Wei, L. Jiao, J. Sun, S. Liu, H. Yuan, *J. Solid State Electrochem.* **2010**, *14*, 197–202.
- [52] H. Zhang, X. Liu, R. Wang, R. Mi, S. Li, Y. Cui, Y. Deng, J. Mei, H. Liu, *J. Power Sources* **2015**, *274*, 1063–1069.
- [53] Z. Hu, X. Zhang, C. Peng, G. Lei, Z. Li, *J. Alloys Compd.* **2020**, *826*, 154055.
- [54] L. Noerochim, J.-Z. Wang, D. Wexler, Z. Chao, H.-K. Liu, *J. Power Sources* **2013**, *228*, 198–205.
- [55] Y. Dong, S. Li, H. Xu, M. Yan, X. Xu, X. Tian, Q. Liu, L. Mai, *Phys. Chem. Chem. Phys.* **2013**, *15*, 17165–17170.
- [56] B. Mendoza-Sánchez, D. Hanlon, J. Coelho, S. O. Brien, H. Pettersson, J. Coleman, V. Nicolosi, *2D Mater.* **2016**, *4*.
- [57] J. Huang, X. Fang, Y. Wu, L. Zhou, Y. Wang, Y. Jin, W. Dang, L. Wu, Z. Rong, X. Chen, X. Tang, *J. Electroanal. Chem.* **2018**, *823*, 359–367.
- [58] C. V. Subba Reddy, Z. R. Deng, Q. Y. Zhu, Y. Dai, J. Zhou, W. Chen, S. I. Mho, *Appl. Phys. A* **2007**, *89*, 995–999.
- [59] V. Madhu Mohan, H. Bin, W. Chen, *J. Solid State Electrochem.* **2010**, *14*, 1769–1775.
- [60] P. Canepa, G. Sai Gautam, D. C. Hannah, R. Malik, M. Liu, K. G. Gallagher, K. A. Persson, G. Ceder, *Chem. Rev.* **2017**, *117*, 4287–4341.
- [61] M. E. Spahr, P. Novák, O. Haas, R. Nesper, *J. Power Sources* **1995**, *54*, 346–351.
- [62] G. Gershinsky, H. D. Yoo, Y. Gofer, D. Aurbach, *Langmuir* **2013**, *29*, 10964–10972.
- [63] T. S. Sian, G. B. Reddy, S. M. Shivaprasad, *Jpn. J. Appl. Phys.* **2004**, *43*, 6248–6251.
- [64] W. Wang, Y. Jiang, Y. Yang, F. Xiong, S. Zhu, J. Wang, L. Du, J. Chen, L. Cui, J. Xie, Q. An, L. Mai, *ACS Nano* **2022**.
- [65] C. Chen, F. Shi, Z.-L. Xu, *J. Mater. Chem. A* **2021**, *9*, 11908–11930.
- [66] a) T. Tojo, H. Tawa, N. Oshida, R. Inada, Y. Sakurai, *J. Electroanal. Chem.* **2018**, *825*, 51–56; b) M. Cabello, F. Nacimiento, R. Alcántara, P. Lavela, C. Pérez Vicente, J. L. Tirado, *Chem. Mater.* **2018**, *30*, 5853–5861.
- [67] T. Das, S. Tosoni, G. Pacchioni, *Comput. Mater. Sci.* **2021**, *191*.
- [68] M. S. Chae, H. H. Kwak, S.-T. Hong, *ACS Appl. Energ. Mater.* **2020**, *3*, 5107–5112.
- [69] a) Z. Liu, Y. Yang, S. Liang, B. Lu, J. Zhou, *Small Structures* **2021**, *2*; b) Z. Xing, Y. Sun, X. Xie, Y. Tang, G. Xu, J. Han, B. Lu, S. Liang, G. Chen, J. Zhou, *Angew. Chem. Int. Ed.* **2023**, *62*, e202215324; c) B. Zhang, L. Qin, Y. Fang, Y. Chai, X. Xie, B. Lu, S. Liang, J. Zhou, *Sci. Bull.* **2022**, *67*, 955–962.
- [70] L. Wang, S. Yan, C. D. Quilty, J. Kuang, M. R. Dunkin, S. N. Ehrlich, L. Ma, K. J. Takeuchi, E. S. Takeuchi, A. C. Marschilok, *Adv. Mater. Interfaces* **2021**, *8*.
- [71] M. R. Dunkin, J. Kuang, S. Yan, S. T. King, L. M. Housel, L. Ma, S. N. Ehrlich, J. S. Okasinski, K. J. Takeuchi, E. S. Takeuchi, A. C. Marschilok, L. Wang, *Adv. Mater. Interfaces* **2022**, *9*.

- [72] H. Zhang, W. Wu, Q. Liu, F. Yang, X. Shi, X. Liu, M. Yu, X. Lu, *Angew. Chem. Int. Ed.* **2021**, *60*, 896–903; *Angew. Chem.* **2021**, *133*, 909–916.
- [73] Y. Liu, J. Wang, Y. Zeng, J. Liu, X. Liu, X. Lu, *Small* **2020**, *16*, e1907458.
- [74] J. Shi, Y. Hou, Z. Liu, Y. Zheng, L. Wen, J. Su, L. Li, N. Liu, Z. Zhang, Y. Gao, *Nano Energy* **2022**, *91*.
- [75] P. Cai, J. Chen, Y. Ding, Y. Liu, Z. Wen, *ACS Sustainable Chem. Eng.* **2021**, *9*, 11524–11533.
- [76] T. Xu, D. Wang, Z. Li, Z. Chen, J. Zhang, T. Hu, X. Zhang, L. Shen, *Nano-Micro Lett.* **2022**, *14*, 126.
- [77] Z. Ma, X. M. Shi, S. I. Nishimura, S. Ko, M. Okubo, A. Yamada, *Adv. Mater.* **2022**, *34*, e2203335.
- [78] H. Guo, D. Goonetilleke, N. Sharma, W. Ren, Z. Su, A. Rawal, C. Zhao, *Cell Rep. Phys. Sci.* **2020**, *1*.
- [79] W. Xu, K. Zhao, X. Liao, C. Sun, K. He, Y. Yuan, W. Ren, J. Li, T. Li, C. Yang, H. Cheng, Q. Sun, I. Manke, X. Lu, J. Lu, *J. Am. Chem. Soc.* **2022**, *144*, 17407–17415.
- [80] H. Lahan, S. K. Das, *J. Power Sources* **2019**, *413*, 134–138.
- [81] R. Tao, C. Gao, E. Xie, B. Wang, B. Lu, *Chem. Sci.* **2022**, *13*, 10066–10073.
- [82] H. Lahan, S. K. Das, *Ionics* **2019**, *25*, 3493–3498.
- [83] B. Jin, S. Hejazi, H. Chu, G. Cha, M. Altomare, M. Yang, P. Schmuki, *Nanoscale* **2021**, *13*, 6087–6095.
- [84] X. He, H. Zhang, X. Zhao, P. Zhang, M. Chen, Z. Zheng, Z. Han, T. Zhu, Y. Tong, X. Lu, *Adv. Sci.* **2019**, *6*, 1900151.
- [85] J. Shi, Y. Hou, Z. Liu, Y. Zheng, L. Wen, J. Su, L. Li, N. Liu, Z. Zhang, Y. Gao, *Nano Energy* **2022**, *91*, 106651.
- [86] H. Zhang, W. Wu, Q. Liu, F. Yang, X. Shi, X. Liu, M. Yu, X. Lu, *Angew. Chem. Int. Ed.* **2021**, *60*, 896–903; *Angew. Chem.* **2021**, *133*, 909–916.
- [87] Y. Liu, J. Wang, Y. Zeng, J. Liu, X. Liu, X. Lu, *Small* **2020**, *16*, 1907458.
- [88] Z. Ma, X.-M. Shi, S.-i. Nishimura, S. Ko, M. Okubo, A. Yamada, *Adv. Mater.* **2022**, *34*, 2203335.
- [89] W. Xu, K. Zhao, X. Liao, C. Sun, K. He, Y. Yuan, W. Ren, J. Li, T. Li, C. Yang, H. Cheng, Q. Sun, I. Manke, X. Lu, J. Lu, *J. Am. Chem. Soc.* **2022**, *144*, 17407–17415.
- [90] H. Guo, D. Goonetilleke, N. Sharma, W. Ren, Z. Su, A. Rawal, C. Zhao, *Cell Rep. Phys. Sci.* **2020**, *1*, 100225.
- [91] X. Wang, Y. Xie, K. Tang, C. Wang, C. Yan, *Angew. Chem. Int. Ed.* **2018**, *57*, 11569–11573; *Angew. Chem.* **2018**, *130*, 11743–11747.
- [92] S.-H. Lee, Y.-H. Kim, R. Deshpande, P. A. Parilla, E. Whitney, D. T. Gillaspie, K. M. Jones, A. H. Mahan, S. Zhang, A. C. Dillon, *Adv. Mater.* **2008**, *20*, 3627–3632.
- [93] J. Hao, J. Zhang, G. Xia, Y. Liu, Y. Zheng, W. Zhang, Y. Tang, W. K. Pang, Z. Guo, *ACS Nano* **2018**, *12*, 10430–10438.
- [94] Y. Zhang, P. Chen, Q. Wang, Q. Wang, K. Zhu, K. Ye, G. Wang, D. Cao, J. Yan, Q. Zhang, *Adv. Energy Mater.* **2021**, *11*.
- [95] S. Wang, H. Zhang, D. Zhang, Y. Ma, X. Bi, S. Yang, *J. Mater. Chem. A* **2018**, *6*, 672–679.
- [96] F. Li, C. R. Cabrera, Z. Chen, *J. Mater. Chem. A* **2014**, *2*, 19180–19188.
- [97] X. Zhao, W. Jia, X. Wu, Y. Lv, J. Qiu, J. Guo, X. Wang, D. Jia, J. Yan, D. Wu, *Carbon* **2020**, *156*, 445–452.
- [98] S. Hu, X. Wang, *J. Am. Chem. Soc.* **2008**, *130*, 8126–8127.
- [99] H. Wei, H.-Y. Yang, X.-Q. Zhang, J.-F. Zhu, P.-P. Qiu, W. Luo, *Tungsten* **2021**, *3*, 338–347.
- [100] Z. Hu, X. Zhang, C. Peng, G. Lei, Z. Li, *J. Alloys Compd.* **2020**, *826*.
- [101] A. Wustrow, J. C. Hancock, J. T. Incorvati, J. T. Vaughney, K. R. Poeppelmeier, *ACS Appl. Energ. Mater.* **2019**, *2*, 2080–2086.
- [102] X. Liu, T. Wang, T. Ji, H. Wang, H. Liu, J. Li, D. Chao, *J. Mater. Chem. A* **2022**, *10*, 8031–8046.
- [103] X. Liu, T. Wang, T. Zhang, Z. Sun, T. Ji, J. Tian, H. Wang, X. Hao, H. Liu, D. Chao, *Adv. Energy Mater.* **2022**, *12*.
- [104] W. Lu, *Int. J. Electrochem. Sci.* **2018**, 275–286.
- [105] W.-X. Huang, Z.-P. Li, D.-D. Li, Z.-H. Hu, C. Wu, K.-L. Lv, Q. Li, *Rare Met.* **2022**, *41*, 3268–3300.
- [106] P. Yan, L. Ji, X. Liu, Q. Guan, J. Guo, Y. Shen, H. Zhang, W. Wei, X. Cui, Q. Xu, *Nano Energy* **2021**, *86*.
- [107] W. Liu, Z. Zhang, J. Shi, Y. Zheng, Y. Wu, X. Fu, N. Liu, J. Su, Y. Gao, *J. Mater. Chem. A* **2022**, *10*, 4043–4052.
- [108] R. Nadimicherla, W. Chen, X. Guo, *Mater. Res. Bull.* **2015**, *66*, 140–146.
- [109] F. Wang, Z. Liu, X. Wang, X. Yuan, X. Wu, Y. Zhu, L. Fu, Y. Wu, *J. Mater. Chem. A* **2016**, *4*, 5115–5123.

Manuscript received: January 8, 2023

Revised manuscript received: March 4, 2023

Accepted manuscript online: March 5, 2023

Version of record online: April 12, 2023